Periodic Mixing of Magmas Recorded by Oscillatory Zoning of the Clinopyroxene Macrocrysts from an Ultrapotassic Lamprophyre Dyke

Chang-Ming Xing[1,2] and Christina Yan Wang[1,2]*

[1]Key Laboratory of Mineralogy and Metallogeny, Guangzhou Institute of Geochemistry, Chinese Academy of Sciences, Guangzhou 510460, China; [2]Guangdong Provincial Key Laboratory of Mineral Physics and Materials, Guangzhou 510640, China

*Corresponding author. Telephone: +86 20 85291803. Fax: +86 20 85291803. E-mail: wang_yan@gig.ac.cn

ABSTRACT

Ultrapotassic rocks are volumetrically minor, but widely distributed in different geological settings. Extensive studies have concerned mantle melting processes that generated these rocks. However, crustal processes that they may have involved are poorly known. In this paper, we describe complex oscillatory zoning patterns of clinopyroxene (Cpx) macrocrysts from an ultrapotassic lamprophyre dyke in the Kyrgyz North Tianshan orogen. These macrocrysts commonly have a corroded or patchy-zoned core surrounded by a mantle with distinct oscillatory zoning, which is, in turn, surrounded by a euhedral rim. The oscillatory zoning of the mantle is composed of alternating coarse and fine layers with a clear resorption surface, or closely packed layers with a straight or wavy boundary in back-scattered electron images. High-amplitude oscillation of Mg#, Ti, Al, Cr and Sr across the layers of the mantle is attributed to magma mixing. Low-amplitude, high-frequency oscillation of Mg# across the closely packed layers was probably developed as a result of kinetic effects or crystal movement under thermal and chemical gradients. In addition, cryptic sector zoning of some macrocrysts clearly shows a Si- and Mg-rich hourglass sector and an Al- and Ti-rich prism sector. The sector zoning indicates crystallization of these macrocrysts under low degrees of undercooling, and the presence of concentric Cr-rich and Cr-poor layers within the same grain indicates that the growth process was disrupted by multiple magma recharging events. The cores of the macrocrysts have Mg# with three distinctive ranges: <84–90 (Core I), 74–84 (Core II) and 60–70 (Core III). The mantles have Mg# ranging from 64 to 90 without a distinct gap. The rims have a narrow range of Mg# from 76 to 80. The cores and mantles with high Mg# ($\geq$85) have variable La/Yb from 1·8 to 5·0 and Dy/Yb from 2·3 to 4·6. The macrocrysts overall have variable $^{87}Sr/^{86}Sr$ from 0·7072 to 0·7084. Highly variable trace elements and $^{87}Sr/^{86}Sr$ within a single grain indicate that both primary and evolved magmas with different compositions were periodically recharged into the crustal magma reservoirs. Modelling results reveal that the melts in equilibrium with the Cpx macrocrysts may have been derived from the magma reservoirs at three different depths equivalent to crystallization pressures of ∼5·4, ∼3·3 and ∼1·6 kbar, respectively, making up a transcrustal magmatic system. The Cpx-laden melts in deep magma reservoirs may have been frequently transported to shallower reservoirs. Magma mixing in the shallower reservoirs led to heterogeneous magmas with different cooling rates and chemical compositions. Early crystallized Cpx crystals were overprinted with diverse zoning patterns during overgrowth and accumulation. Thus, the complex zoning patterns and compositions of the Cpx macrocrysts have important implications for a transcrustal magmatic system in the formation of ultrapotassic rocks.

Key words: oscillatory zoning; clinopyroxene; lamprophyre; ultrapotassic rocks

INTRODUCTION

Lamprophyre is a field term for alkali-rich, porphyritic dykes with essentially primary amphibole and/or mica phenocrysts, and is typified by the absence of felsic phenocrysts and groundmass olivine (Rock, 1977). Lamprophyres are actually a wide variety of hypabyssal rocks with diverse mineral assemblages (Rock, 1977, 1984, 1986, 1987, 1991). Ultrapotassic lamprophyres are unique and have chemical compositions different from mafic dykes in the same region (Venturelli *et al.*, 1984; Owen, 2008). Ultrapotassic rocks are defined to have >3 wt% K_2O, >3 wt% MgO and K_2O/Na_2O >2 (Foley *et al.*, 1987). They are volumetrically minor relative to terrestrial basaltic rocks despite their wide distribution in orogenic belts and within-plate settings. However, they carry important messages about the nature of the mantle, mantle processes such as partial melting and metasomatism, and post-collisional geodynamic processes associated with magma upwelling (Conticelli & Peccerillo, 1992; Foley, 1992*a*, 1992*b*; Prelević *et al.*, 2005, 2008, 2012; Huang *et al.*, 2010; Muravyeva *et al.*, 2014; Ammannati *et al.*, 2016; Gülmez *et al.*, 2016; Soder & Romer, 2018).

Ultrapotassic rocks are rich in incompatible elements and volatiles and have highly variable compositions of radiogenic isotopes (Foley, 1987, 1992*a*). Phenocrysts of mica, amphibole and clinopyroxene in these rocks are commonly zoned with highly variable compositions (Venturelli *et al.*, 1984; Prelević *et al.*, 2004, 2005; Huang *et al.*, 2010; Muravyeva *et al.*, 2014; Gülmez *et al.*, 2016). The complexity of mineralogy and whole-rock compositions makes it impossible to explain the origin of ultrapotassic rocks with a simple model (Miller *et al.*, 1999). The formation of ultrapotassic rocks may be controlled by multiple factors: the evolution and mineral assemblages of the mantle, degrees of partial melting of the mantle, fractionation and crustal contamination of magmas, and particularly mixing or mingling processes of magmas from different mantle sources under different physicochemical conditions (Foley, 1992*a*, 1992*b*; Miller *et al.*, 1999; Prelević *et al.*, 2004, 2005, 2008, 2012; Huang *et al.*, 2010; Muravyeva *et al.*, 2014; Ammannati *et al.*, 2016; Gülmez *et al.*, 2016; Soder & Romer, 2018). However, the dynamics and architecture of plumbing and storage systems and the magma mixing processes in the crustal magma reservoirs were rarely reported in earlier studies, despite intense studies on the magma sources of ultrapotassic rocks.

Geophysical, geochemical and petrological observations in many large volcanic fields have revealed that a shallower magma reservoir may be a volumetrically minor part of a large, vertically extended magmatic system that comprises many deeper magma reservoirs in a transcrustal magmatic system (Cashman *et al.*, 2017; Sparks & Cashman, 2017). Complete mixing of melts from different mantle sources in the lower crust or deep mixing of channelized melt flows in the mantle could lead to the homogeneity of magmas before they are transported and pooled in the shallower magma reservoirs (Maclennan, 2008; Rudge *et al.*, 2013; Jennings et al., 2017). On the other hand, mixing of compositionally different magmas in the shallower magma reservoirs is commonly incomplete, resulting in highly variable compositions of magmas and extremely complex zoning patterns of minerals (Humphreys, 2006; Ginibre & Wörner, 2007). However, our understanding of ultrapotassic magmatic systems in the crust is still limited; few studies so far have referred to the crystallization pressure of phenocrysts in ultrapotassic rocks (Prelević *et al.*, 2012). It remains enigmatic how the magmatic system influences the evolution of ultrapotassic magmas and how ultrapotassic melts mix and fractionate in the crustal magma reservoirs.

Phenocrysts in volcanic rocks record the physicochemical conditions of crystallization and the dynamics of magma upwelling and mixing prior to eruption (Ginibre *et al.*, 2007; Streck, 2008; Cooper, 2017; Ubide *et al.*, 2019*a*). Multiple crystal populations can be gathered and mingled with their host melts in an open magmatic system, leading to textural and compositional diversity of crystals (Humphreys *et al.*, 2006; Ginibre & Wörner, 2007; Martin *et al.*, 2010; Cooper, 2017). Lamprophyre dykes can host abundant phenocrysts, antecrysts and xenocrysts with distinct zoning patterns, which can record a complex history during magma ascent (O'Brien et al., 1988; Ubide *et al.*, 2014). Such complex zoning patterns may provide a window to study magmatic processes in the plumbing and storage system.

In this paper, we describe zoning patterns of clinopyroxene (Cpx) macrocrysts from an ultrapotassic lamprophyre dyke in the Kyrgyz North Tianshan orogen. These macrocrysts display complex oscillatory zoning, patchy zoning, sieve texture and cryptic sector zoning. We document the within-grain compositional variation, Mg# profiles based on grey-values extracted from back-scattered electron (BSE) images and *in situ* trace element and Sr isotopic compositions of the macrocrysts. A multi-sourced magma mixing model is proposed to explain the origin of the Cpx macrocrysts. This study highlights that ultrapotassic magmas could be a mixture of magmas from different mantle sources and contain multiple crystal populations that are probably spatially or temporally isolated in a transcrustal magmatic system before they are transported to a shallower magma reservoir.

PETROGRAPHY OF THE LAMPROPHYRE DYKE

The Kyrgyz North Tianshan orogen is part of the southern margin of the central Asia orogenic belt (CAOB) (Fig. 1a). A series of late Paleozoic K-rich igneous rocks formed in the Tianshan orogen as a result of the northward subduction of the Tianshan oceanic plate beneath the Kazakhstan–Yili plate (Biske *et al.*, 2013; Yang *et al.*, 2014). The Tarim microcontinent approached the subduction zone in the southern margin of the Kazakhstan
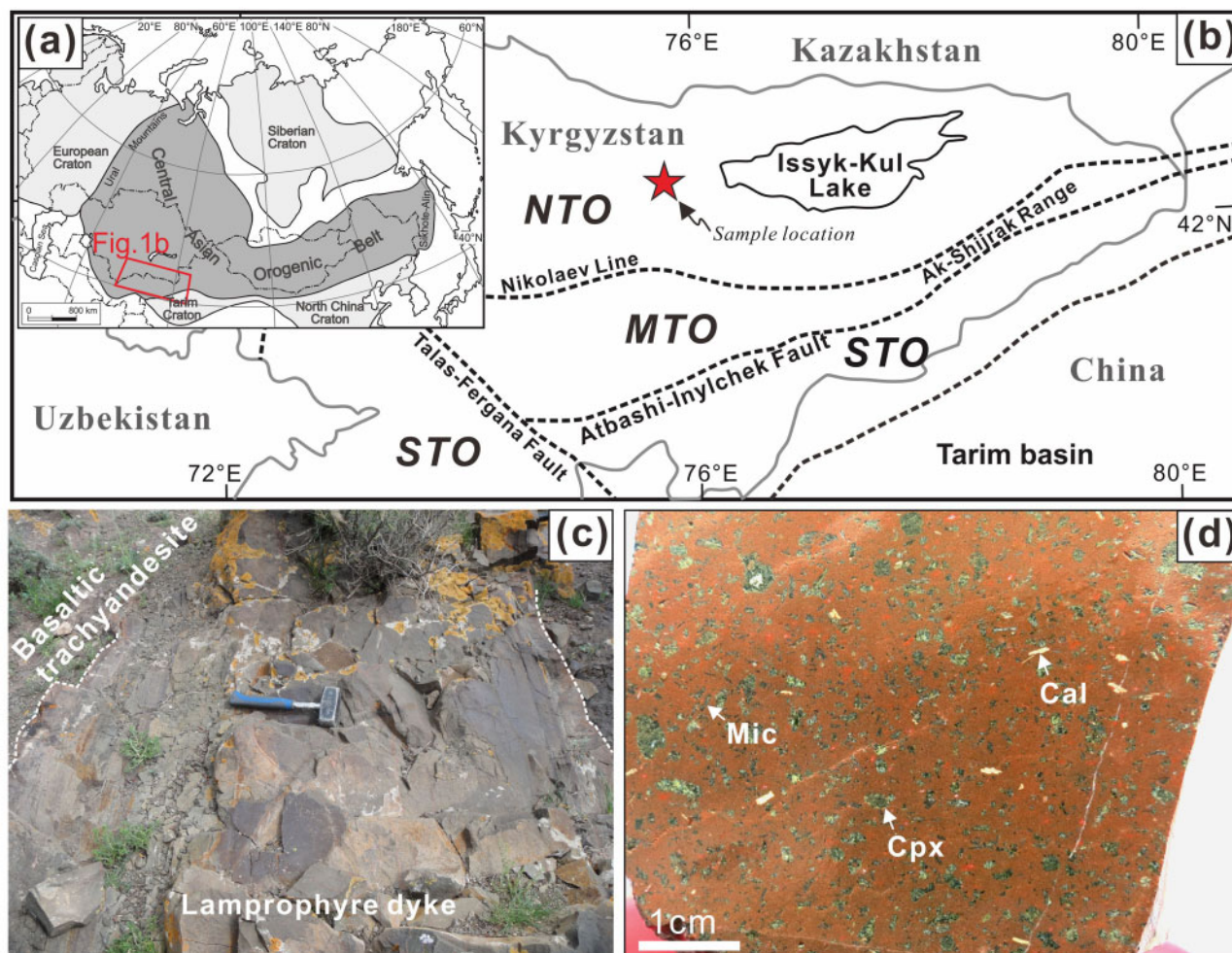
Fig. 1. A simplified geological map showing the distribution of the central Asian orogenic belt (a) and the location of the ultrapotassic lamprophyre dyke in the North Tianshan orogen, Kyrgyzstan (b). Field outcrop (c) and sliced section (d) of the lamprophyre dyke showing the trachyandesitic wall-rock and major minerals clinopyroxene (Cpx) and mica (Mic), and minor secondary calcite (Cal) replacing mica. (a) is modified from Han *et al.* (2011) and Cao *et al.* (2019); (b) is modified after Konopelko *et al.* (2013). NTO, MTO and STO denote the North, Middle and South Tianshan orogenic belt, respectively.

microcontinent in the late Carboniferous, leading to continent–continent collision in the early Permian (Djenchuraeva, 2005). Permian K-rich igneous rocks that were produced by partial melting of the metasomatized mantle wedge are widely distributed in the Chinese West Tianshan orogen (Yang *et al.*, 2014).

An ultrapotassic lamprophyre dyke intrudes the early Permian basaltic trachyandesite in the Ortok Mountain area, Kyrgyzstan (Fig. 1b). This lamprophyre dyke is about 1·5 m in width (Fig. 1c) and extends for hundreds of meters along-strike. The rocks of the dyke are reddish-brown in color and display porphyritic texture. They can be defined as minette (Rock, 1977), and contain up to *c*. 30 vol% macrocrysts of clinopyroxene and mica and 65–70 vol% groundmass, as well as minor glassy matrix (<5%) and carbonate ocelli (<1%), and negligible vesicles and amygdales (Fig. 1d).

The macrocrysts of clinopyroxene and mica sometimes assemble to form polymineralic glomerocrysts (Fig. 2a). The mica macrocrysts are generally 0·2–2 mm

in length and have a euhedral grain boundary in contact with the groundmass. They are commonly intensely altered and partially replaced by chlorite, calcite and minor epidote (Fig. 2a–c). The Cpx macrocrysts are euhedral and mostly elongated in thin sections, and range in length from 0·2 to 4 mm (Fig. 2). Hexagonal or needle-like apatite grains are sporadically enclosed within the Cpx macrocrysts, and range in length from 20 to 150 μm (Fig. 2b). The Cpx macrocrysts commonly display complex zoning patterns composed of alternating green and white layers as seen in plane-polarizer micrographs (Fig. 2b). They show clear oscillatory zoning (Fig. 2a–c), sieve texture (Fig. 2d) and patchy zoning (Fig. 2e). Some Cpx macrocryts with patchy zoning contain abundant melt inclusions with different color (Fig. 2f).

Microcrysts of K-feldspar, albite and magnetite make up 88–95 vol% of the groundmass. The K-feldspar and albite microcrysts are generally 100–200 μm in length, and the magnetite microcrysts have grain sizes ranging
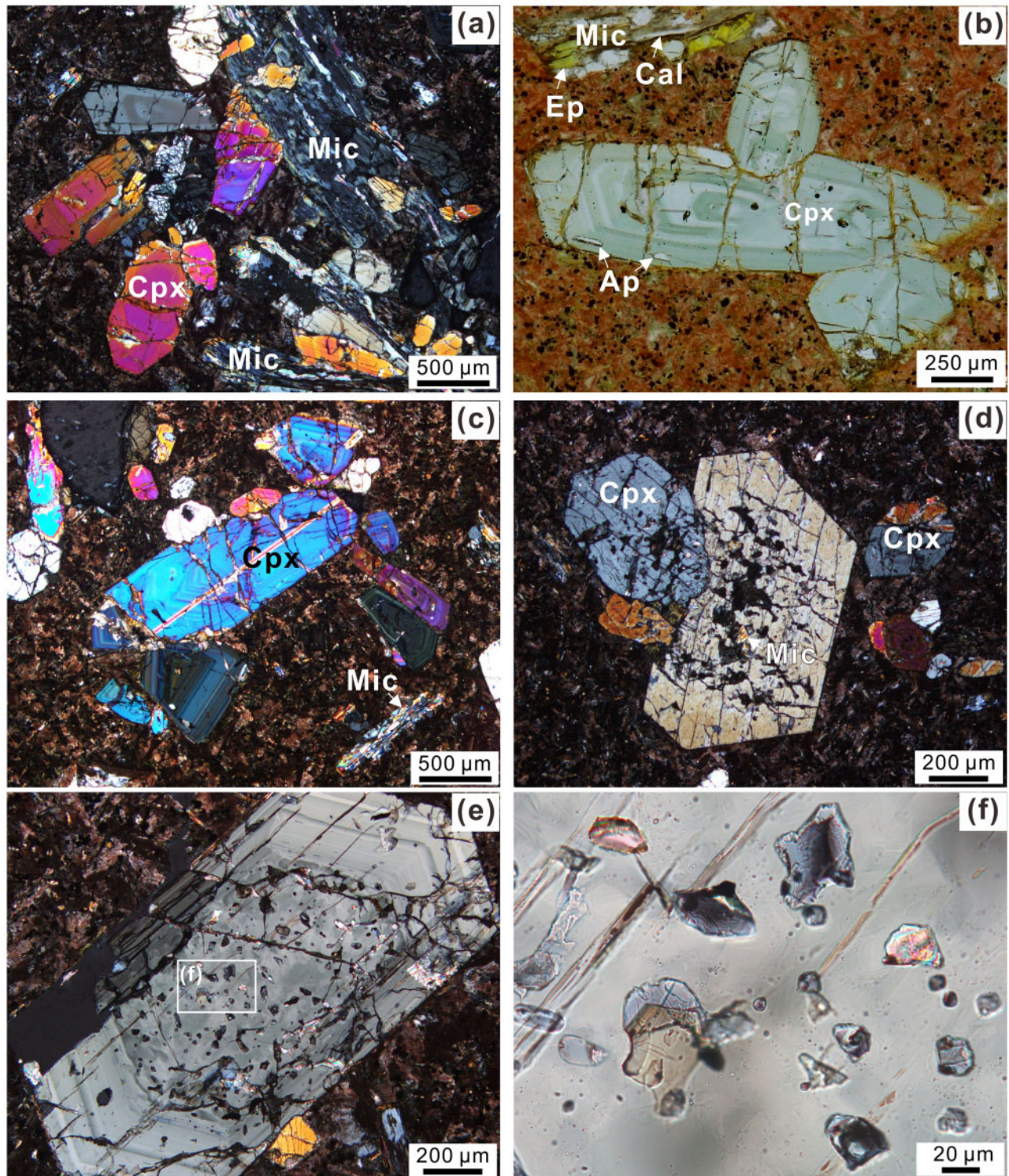
Fig. 2. Photomicrographs of the Cpx macrocrysts from the lamprophyre dyke. (a) Micrograph (cross-polarized light) showing poly-mineralic glomerocrysts of clinopyroxene (Cpx) and mica (Mic). It should be noted that the mica is altered to chlorite. (b) Micrograph (plane-polarized light) showing distinct oscillatory zoning of the Cpx macrocryt that consists of concentric green and white layers. A mica in the upper part is partially replaced by epidote (Ep) and calcite (Cal). (c) Micrograph (cross-polarized light) showing multiple Cpx macrocrysts with clear oscillatory zoning. (d) Micrograph (cross-polarized light) showing distinct sieve texture in the cores of the Cpx macrocrysts. (e) Micrograph (cross-polarized light) showing patchy zoning in the core of a Cpx macrocryst and oscillatory zoning in the mantle. (f) Close-up of (e) showing abundant melt inclusions with different colors.

from 10 to 30 μm. The groundmass also contains minor microcrysts of clinopyroxene (5–8 vol%) and mica (∼3 vol%). The Cpx microcrysts usually have grain sizes <50 μm, and occur as discrete grains with simple zoning. The mica microcrysts are needle-shaped and generally range from 50 to 100 μm in length.

ZONING PATTERNS OF CPX MACROCRYSTS

Almost all the Cpx macrocrysts in the lamprophyre dyke are oscillatory-zoned, and some of them have distinct patchy zoning or coarse-scale sieve texture in the core (Figs 3 and 4). At thin-section scale, the macrocrysts with sieve texture are usually less than 5 vol%. For simplicity, typical Cpx macrocrysts refer to those without sieve texture in this study.

Oscillatory zoning

Oscillatory zoning in the Cpx macrocrysts is characterized by multiple, concentric growth layers in the mantles (Fig. 3). The cores are generally irregular in shape and show either dark or bright color in BSE images (Fig. 3a and b), and they sometimes show patchy zoning (Fig. 3c), or multiple cores within a crystal (Fig. 3d). The rims of these macrocrysts show euhedral outlines (Fig. 3).

The mantles of the Cpx macrocrysts develop asymmetrically different types of growth layers (Fig. 3). The Cpx macrocrysts constituting a glomerocryst may share similar zoning patterns (Fig. 3a), or show distinctly different patterns in the mantle (Fig. 3e). A single crystal commonly has a mantle composed of 10–50 alternating coarse and fine layers with highly variable thickness. The layers that grow along the *c*-axis are generally thicker than the others (Fig. 3a, c and d). It is noted that both coarse and fine layers are commonly resorbed. The resorption surface can crosscut either several growth layers or just a single layer, and is denoted as a major (R) and minor (r) resorption surface, respectively (Ginibre *et al.*, 2002*a*, 2002*b*). The R surface appears either as rounded edges at crystal corners (R_1 in Fig. 3f and g), or intruding fingers along the long crystal face (R_2 in Fig. 3f), or as a sawtooth shape along the short crystal face (R_3 in Fig. 3f). The r surface commonly has a wavy boundary on one side and a straight boundary on the other side of a layer (r in Fig. 3f). In addition, some macrocrysts are mainly composed of coarse layers (Fig. 3a), whereas others are characterized by a suite of closely packed layers with thickness less than 30 μm (Fig. 3f). These closely packed layers show either a straight or wavy boundary in contiguous layers. Some glomerocrysts are closely interlocked with different zoning patterns in the core, but show continuous, concentric layers in the mantle and rim (Fig. 3g and h).

Patchy zoning and sieve texture

Patchy zoning and sieve texture mainly occur in the core of the Cpx macrocrysts (Fig. 4a–c). The patchy zoning shows highly irregular bright and dark domains in BSE images and melt inclusions are scattered mainly in the dark domains (Fig. 4a). The sieve texture generally shows patchy-zoned Cpx and spongy spaces filled with mica and matrix materials, which are connected with groundmass through cracks (Fig. 4b and c). However, the sieve texture may also occur randomly in some macrocrysts with abundant mica inclusions and minor matrix (Fig. 4e and f). Several sieved macrocrysts may assemble to form remarkable 'snowflake' glomerocrysts, in which continuous, concentric layers can be traced across individual grains (Fig. 4e and f).

ANALYTICAL METHODS

Whole-rock major and trace elements and Sr–Nd isotope analyses

Whole-rock major elements and Sr–Nd isotopes were analyzed at the State Key Laboratory of Isotope Geochemistry, Guangzhou Institute of Geochemistry (GIG), Chinese Academy of Sciences (CAS). The samples were crushed into small fragments before being further cleaned with deionized water in an ultrasonic bath and then powdered in a corundum mill. Whole-rock major oxide analysis was carried out using a Rigaku RIX 2000 X-ray fluorescence spectrometer. Samples were prepared as glass discs and analyzed following the procedure described by Goto & Tatsumi (1996). Analytical uncertainties for major elements are lower than 5%.

Whole-rock trace elements were determined by inductively coupled plasma mass spectrometry (ICP-MS) using a PEELAN 9000 system in the Institute of Geochemistry, CAS, following the method of Qi & Grégoire (2000) and Qi *et al*. (2000). The uncertainties of ICP-MS analyses are estimated to be better than 5–10% (relative) for most elements.

Whole-rock Sr–Nd isotopes were analyzed using a Neptune Plus multicollector (MC)-ICP-MS system. For Sr and Nd isolation and purification, 100 mg sample powders were initially dissolved by HF + HNO_3 acid in Teflon capsules. After sample decomposition, Sr and rare earth element (REE) were separated using cation exchange columns, and then the Nd fractions were further separated using HDEHP-coated Kef columns. The analytical methods for Sr–Nd isotopes follow the procedure of Wei *et al*. (2002) and Liang *et al*. (2003). Normalizing factors used to correct the mass fractionation of Sr and Nd during the measurements are $^{86}Sr/^{88}Sr = 0.1194$ and $^{146}Nd/^{144}Nd = 0.7219$. The whole-rock major and trace elements and Sr–Nd isotopic compositions are listed in Supplementary Data Table S1 (supplementary data are available for downloading at http://www.petrology.oxfordjournals.org).

Clinopyroxene major and trace element analyses

Major and trace element compositions of clinopyroxene were analyzed at the Key Laboratory of Mineralogy and
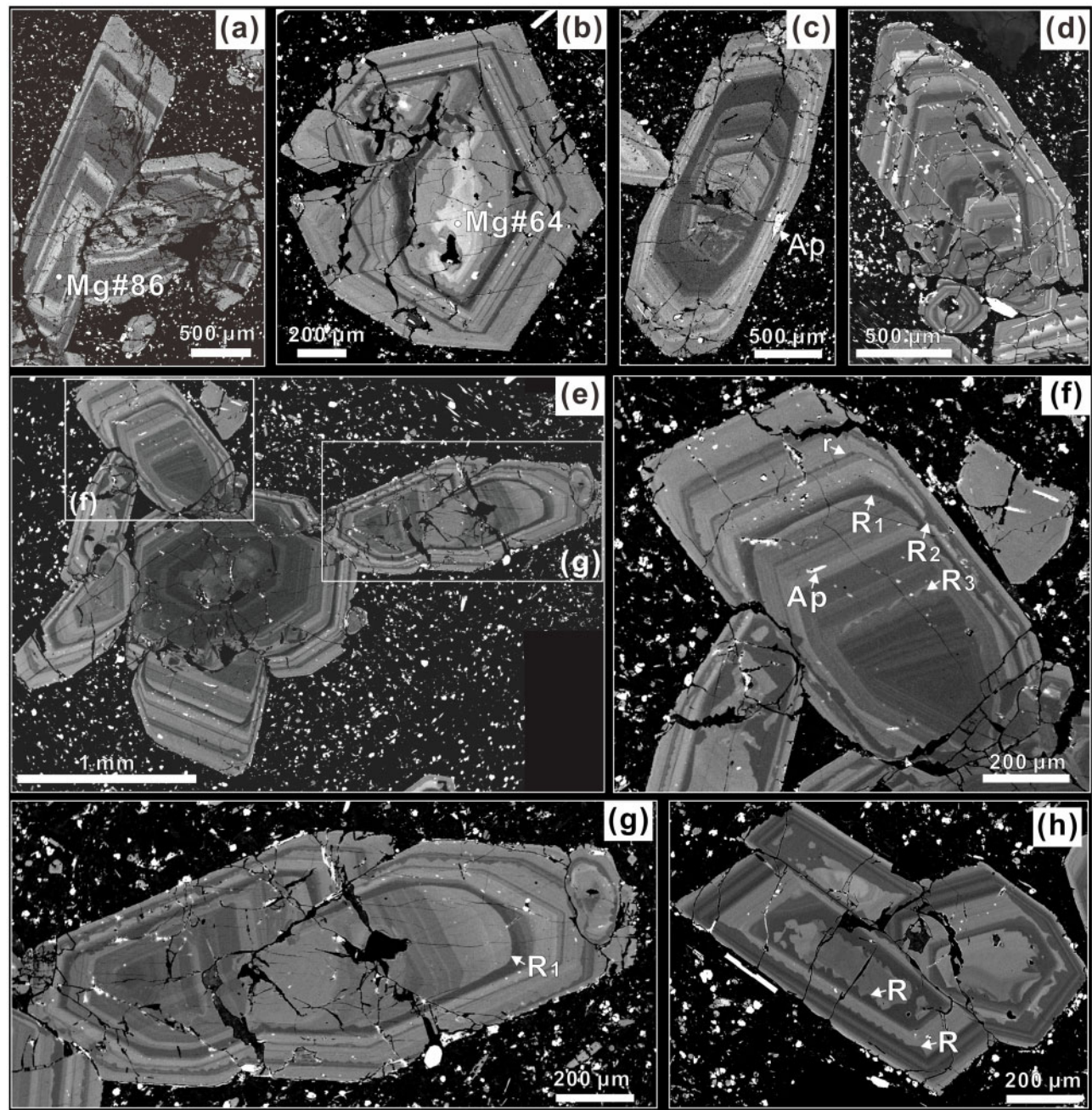
Fig. 3. Back-scattered electron images of the Cpx macrocrysts with oscillatory zoning from the lamprophyre dyke. (a) A dark core and multiple coarse layers in the mantle. (b) A bright core and multiple fine layers in the mantle. (c) A patchy-zoned core and both coarse and fine layers in the mantle. (d) Multiple cores within a grain. (e) Distinctively different patterns of zoning in each Cpx macrocryst. (f) Close-up of (e) showing remarkable major resorption surface (R), such as rounded corner (R1), intruding fingers (R2) and sawtooth boundaries (R3), and obscure minor resorption surface (r). The Cpx macrocrysts sometimes contain fine-grained apatite (Ap) inclusions (f). (g, h) Cpx glomerocrysts showing different zoning patterns in the core and similar zoning patterns in the mantle and rim. It should be noted that the concentric layers in the mantle and rim can be traced across different grains.

Metallogeny, GIGCAS. Major elements were determined using a JEOL JXA-8230 electron probe micro-analyzer (EPMA). Operating conditions of 15 kV, 20 nA and a 1 μm beam were applied to the analyses for all elements. Peak, upper and lower background counting times were 20, 10 and 10 s for Si, Fe, Mg and Ca, 40, 20 and 20 s for Ti and Mn, 60, 30 and 30 s for Cr, and 10, 5 and 5 s for Na. Analytical results were reduced using the ZAF (Z, atomic

number; A, absorption; F, fluorescence) correction routines. Standards used during quantitative calibration were chrome-diopside for Si and Ca, olivine for Mg, magnetite for Fe, almandine garnet for Al, rutile for Ti, rhodonite for Mn, Cr_2O_3 for Cr and albite for Na. Chrome-diopside from SPI supplies was used as a quality monitor standard for the calculation of accuracy and precision. Accuracy was <3 % for major elements (≥1 wt%) and
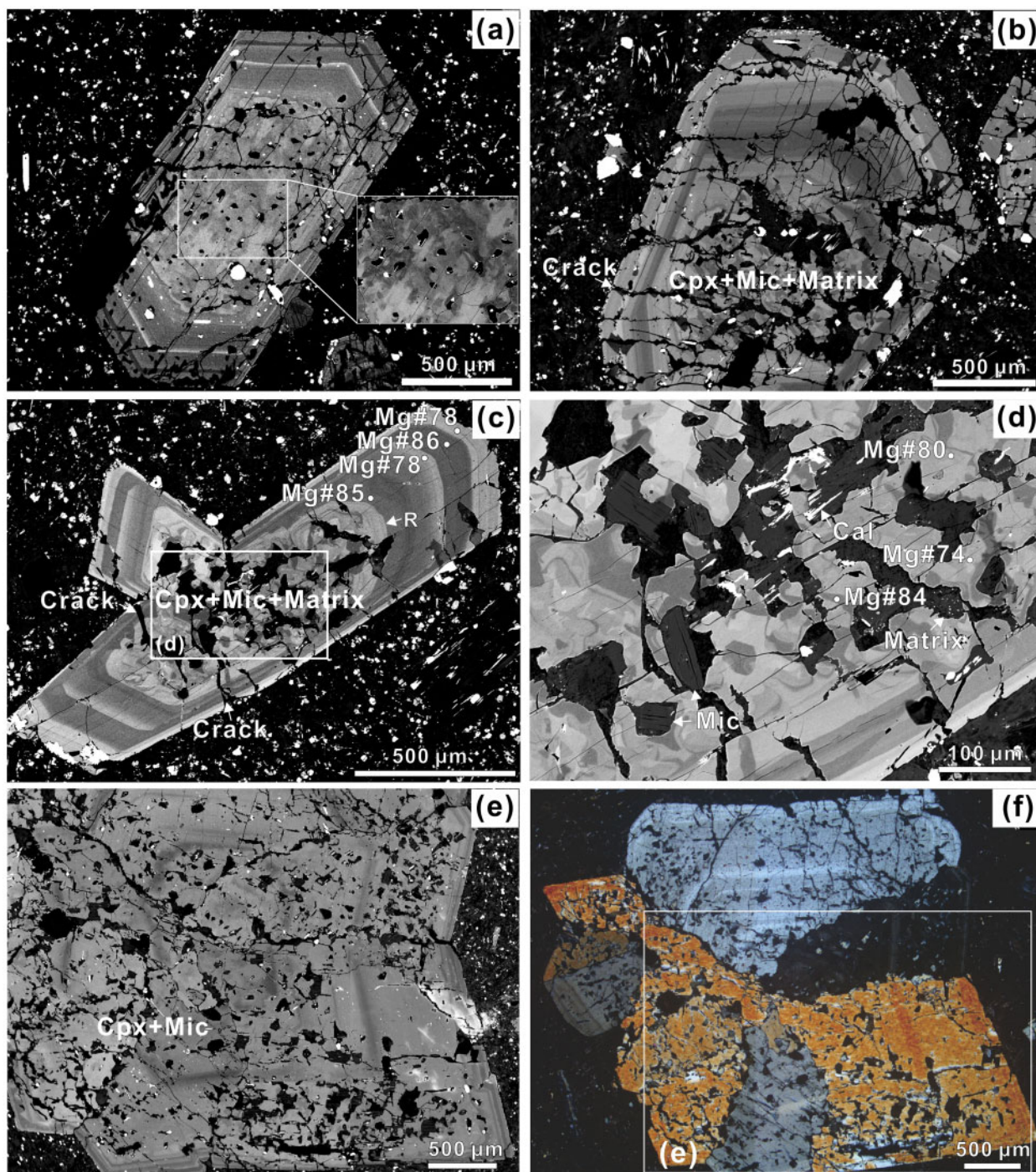
Fig. 4. Back-scattered electron images and photomicrograph of the Cpx macrocrysts with patchy zoning and sieve texture from the lamprophyre dyke. (a) The patchy zoning shows highly irregular bright and dark domains in the core. The inset shows abundant melt inclusions in the dark domains. (b, c) The sieve texture showing a patchy-zoned core with abundant spongy spaces, which are filled with mica and matrix materials. It should be noted that the crack connects the groundmass and sieved core. (d) Close-up of (c) showing irregular bright and dark domains in the patchy-zoned core. (e) Close-up of (f) showing the Cpx macrocryst with sieve texture and concentric zoning. It should be noted that the concentric layers do not show evident resorption and can be traced between different grains.

<10% for minor elements (<1 wt%), and 1σ precision was <3% and <15% for major and minor elements, respectively. The full dataset of major and minor elements of clinopyroxene and the standard are shown in Supplementary Data Table S2.

Trace element compositions of clinopyroxene were analyzed by laser ablation (LA)-ICP-MS. An Agilent 7900a ICP-MS instrument was coupled to a Resonetic 193 nm ArF excimer laser ablation system. Single spot ablation mode was adopted with a laser beam of 43 μm.

Laser energy was 120 mJ and ablation frequency was 6 Hz. Helium gas was used as a carrier gas and nitrogen gas as an additional gas to enhance sensitivity. Prior to analysis, the LA-ICP-MS system was optimized using NIST 610 glass to achieve the maximum signal intensity and low oxide rates. Multiple glass reference materials (BCR-2G, BHVO-2G, BIR-1G and GOR132-G) were used as external calibration references and monitor standards and Ca content determined by EPMA was used as the internal standard to quantify elemental concentrations. Data reduction was performed using the ICPMSDataCal software (version 10.2) (Liu *et al.*, 2008; Lin *et al.*, 2016). The detection limit is lower than 0·1 ppm for most trace elements and the relative uncertainty is better than 10 %. Trace element compositions of clinopyroxene are shown in Supplementary Data Table S3. The measured trace element concentrations of reference materials and their recommended values are listed in Supplementary Data Table S4.

Clinopyroxene in situ *Sr isotope analysis*

In situ Sr isotopic analysis for clinopyroxene was performed on a Neptune Plus MC-ICP-MS system (Thermo Scientific), coupled with a RESOlution M-50 193 nm laser ablation system (Resonetics) at the State Key Laboratory of Isotope Geochemistry, GIGCAS. A small N_2 flow (2 ml l^{-1}) and an X skimmer cone in the interface were used to improve the instrumental sensitivity. All isotopic signals were determined by Faraday cups under the static mode. The diameter of the laser beam was 155 μm and ablation rate was 6 Hz with an energy density of ∼4 J cm^{-2}. Helium gas was used as the carrier gas. Each analysis consisted of 250 cycles with an integration time of 0·262 s per cycle. The first 30 s was used to detect the gas blank with the laser beam off, followed by 30 s laser ablation on the samples. During the analyses, the gas blank of ^{83}Kr and ^{88}Sr was less than 2·5 mV and 0·5 mV, respectively. The interferences of ^{84}Kr and ^{86}Kr on ^{84}Sr and ^{86}Sr were corrected by subtracting the gas blank from the raw time-resolved signal intensities. ^{85}Rb was used to correct the interference of ^{87}Rb on ^{87}Sr with a natural ^{85}Rb/^{87}Rb ratio of 2·593 (Catanzaro *et al.*, 1969). The mass bias of ^{87}Sr/^{86}Sr was normalized to ^{86}Sr/^{88}Sr = 0·1194 with an exponential law. The detailed analysis and data reduction procedure have been documented by Zhang *et al.* (2018). In this study, nine analyses of NKT-1G (a basaltic glass) during the course yielded a weighted mean ^{87}Sr/^{86}Sr of 0·70351 ± 0·00007 (2σ), which is consistent within error with the results reported by Elburg *et al.* (2005). The Sr isotopic composition of clinopyroxene is shown in Supplementary Data Table S5.

Grey-value profiles of clinopyroxene extracted from BSE images

High-resolution compositional profiles of minerals are generally acquired by EPMA, which can yield profiles with point intervals of several microns. However, this technique may be time consuming for millimeter-scale or even larger grains (Ginibre *et al.*, 2002*a*). Recently, it has been demonstrated that grey values extracted from BSE images of clinopyroxene are highly correlated with Mg# of clinopyroxene (Petrone *et al.*, 2016, 2018). Comparing with compositional profiles obtained by EPMA, the grey-value profiles extracted from BSE images could have higher spatial resolution (<1 μm).

To better confine the Mg# variations in both coarse and fine layers of clinopyroxene in our samples, we took high-contrast BSE images of clinopyroxene using the JEOL JXA-8230 EPMA. The BSE images were further edited by enhancing image contrast so that the differences in grey values can be optimized. The grey-value profiles of clinopyroxene were then extracted from the enhanced BSE images using the image processing software of ImageJ (version 1.44p) (https://imagej.nih.gov/ij/). Each grey-value profile was then calibrated with the actual compositions of clinopyroxene obtained by EPMA. Comparing with the Mg# calculated based on EPMA results, the uncertainty for the converted Mg# from the grey values is generally lower than 1·5 %.

High-resolution 2-D elemental distribution maps of clinopyroxene

High-resolution 2-D elemental X-ray mapping was applied for two Cpx macrocrysts. The mapping was carried out using the same EPMA at GIG, CAS. Operation conditions of accelerating voltage of 20 kV, probe current of 50–150 nA and beam size of 2–4 μm were adopted for mapping. The dwell-time was set to be 100 ms for each point. Mg Kα, Al Kα, Si Kα and Na Kα were analyzed using a TAP crystal. Fe Kα and Ti Kα were analyzed using an LIF crystal. Ca Kα was analyzed using a PETJ crystal and Cr Kα was analyzed using an LIFH crystal.

RESULTS

Whole-rock major and trace element and Sr–Nd isotope composition

The rocks from the lamprophyre dyke contain ∼52 wt% SiO_2, 6·74–6·89 wt% MgO and 5·66–6·37 wt% K_2O with K_2O/Na_2O >2 (Supplementary Data Table S1). They have up to 14 wt% Al_2O_3 and K_2O/Al_2O_3 of ∼0·4, similar to Group III (Roman province type) ultrapotassic rocks in the orogenic belts (Foley *et al.*, 1987).

The rocks show light rare earth element (LREE)-enriched and heavy rare earth element (HREE)-depleted patterns in the chondrite-normalized REE diagram, similar to those for the ocean island basalt (OIB; Sun & McDonough, 1989) and global subducting sediment (GLOSS; Plank & Langmuir, 1998) (Supplementary Data Fig. S1). In the primitive mantle-normalized trace element patterns, the rocks show positive anomalies of Rb, Ba, Th and U, and negative anomalies of Nb, Ti, Zr, Hf and Sr, similar to GLOSS (Supplementary Data Fig. S1).

The rocks have $^{87}Sr/^{86}Sr$ ranging from 0·7109 to 0·7115 and nearly constant $^{143}Nd/^{144}Nd$ of 0·5124–0·5125 (Supplementary Data Table S1). As the ultrapotassic lamprophyre dyke in the Ortok Mountain area intrudes early Permian basaltic trachyandesite, we adopt 290 Ma to calculate the initial $^{87}Sr/^{86}Sr$ and $\varepsilon_{Nd(t)}$, which range from 0·7053 to 0·7089 and from –3·2 to –1·7, respectively.

Overall compositional variation of Cpx macrocrysts

The Cpx macrocrysts of the lamprophyre dyke have compositions of $En_{30-47}Fs_{6-20}Wo_{45-50}$, falling into the diopside field according to the classification scheme of Morimoto (1988) (Supplementary Data Fig. S2). They have highly variable Mg# [Mg# = 100Mg/(Mg + Fe$_{total}$)] and major and minor element contents, even at a single crystal scale (Figs 5 and 6; Supplementary Data Table S2). The cores of the Cpx macrocrysts have Mg# varying from 61 to 89 and clearly show three groups of Mg# in the histogram, Core I, II and III, with a remarkable gap between Core II and III (Fig. 5a). Core I has Mg# varying from 84 to 90 with a peak at 86–88, Core II has Mg# varying from 74 to 84 with a peak at 76–80, and Core III has Mg# varying from 60 to 70 without an obvious peak (Fig. 5a). The oscillatory zoned mantles have a similar range of Mg# (65–90) to that of the cores but without an obvious gap (Fig. 5b). The rims have a restricted Mg# range with a peak at 76–80, similar to that of Core II (Fig. 5c). The sieved domains of the Cpx macrocrysts have Mg# varying from 66 to 86, with a peak at 76–80 (Fig. 5d). The Cpx microcrysts in the groundmass have Mg# varying from 66 to 78 with a peak at 70–74 (Fig. 5e).

The cores and mantles of the Cpx macrocrysts have similarly variable Cr_2O_3 contents (Fig. 6a) and display negative correlation of Mg# with TiO_2, Al_2O_3 and Na_2O (Fig. 6b–d). In contrast, the rims show restricted Cr_2O_3, TiO_2, Al_2O_3 and Na_2O contents (Fig. 6). The sieved domains of the Cpx macrocrysts and the Cpx microcrysts have scattered major oxide contents, obviously deviating from the trends of the core and mantle (Fig. 6).

The trace element compositions of a single grain or among different Cpx macrocrysts are highly variable (Supplementary Data Table S3). The core and rim of a single grain may show restricted ranges of trace elements, in contrast to a one order of magnitude variation for the mantle (Fig. 7). Overall, they have chondrite-normalized REE patterns with a weakly negative Eu anomaly (Fig. 7a), and very negative Ti and Ni anomalies, a positive Sc anomaly and variable degrees of negative Sr, Zr and Hf anomalies in primitive mantle-normalized trace element patterns (Fig. 7b). In binary plots of Cpx Mg# versus V/Sc, La/Yb and Dy/Yb, all data are scattered in a wide range (Fig. 8). In particular, the cores and mantles of the Cpx macrocrysts have V/Sc
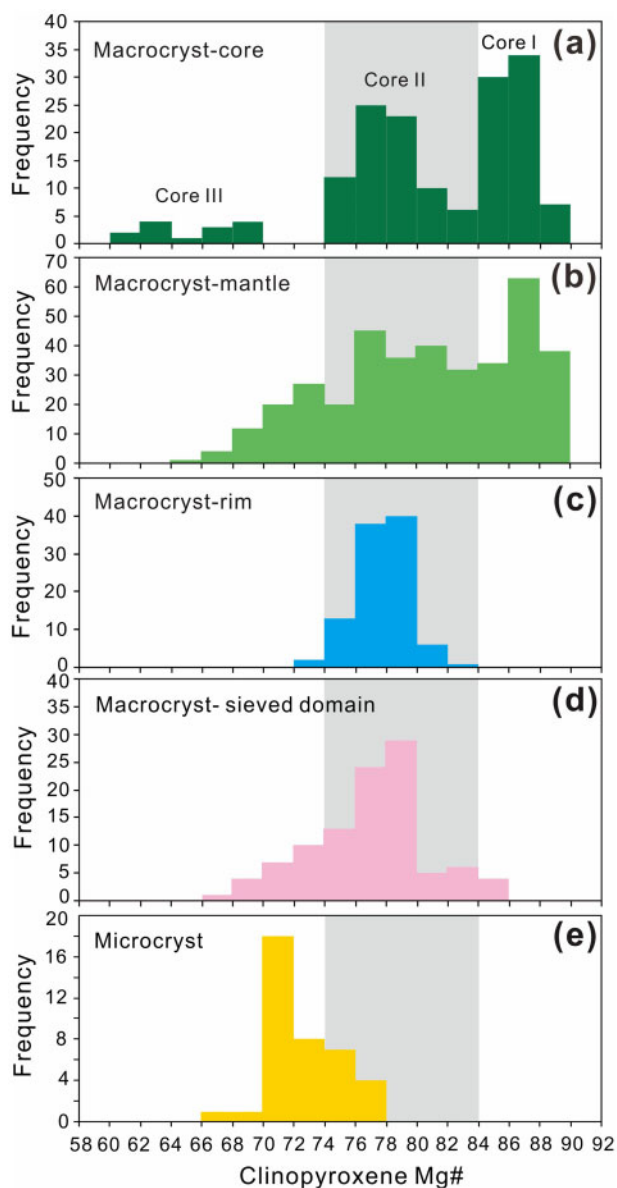

Fig. 5. Histograms of Cpx Mg# [Mg# = 100Mg/(Mg + Fe)] for the Cpx macrocrysts (a–d) and microcrysts in the groundmass (e) of the lamprophyre dyke.

varying from 1·1 to 2·3, La/Yb from 1·8 to 5·0 and Dy/Yb from 2·3 to 4·6 against Mg# from 90 to 85 (Fig. 8).

2-D elemental maps of Cpx macrocrysts

The Cpx macrocrysts show clear oscillation of Fe, Mg, Al, Ti, Cr, Na, and Si in the coarse and fine layers and distinct sector zoning in the high-resolution 2-D elemental maps (Figs 9 and 10). It is noted that sector zoning is not observed in BSE images. The layers in the hourglass sector are relatively enriched in Si and Mg, whereas the layers in the prism sector are intensely enriched in Al and Ti and weakly enriched in Na (Figs 9 and 10). All the layers do not show clear sector zoning of Cr and Fe (Fig. 10e and f). In addition, the maps reveal that the closely packed layers with wavy boundaries show
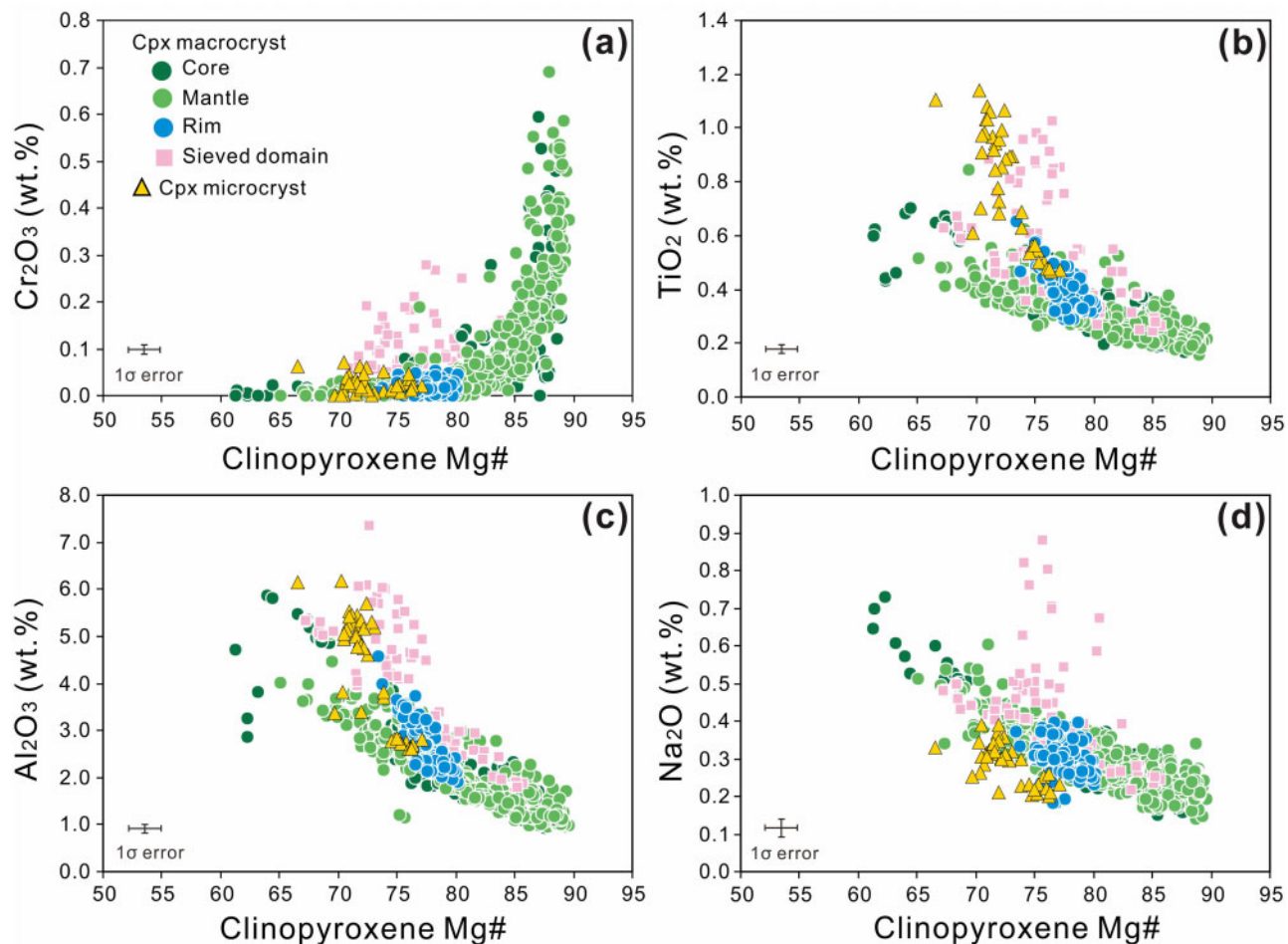
Fig. 6. Binary plots of Mg# vs Cr₂O₃ (a), TiO₂ (b), Al₂O₃ (c) and Na₂O (d) contents of Cpx from the lamprophyre dyke. The error bars show one standard deviation of analysis by EPMA.
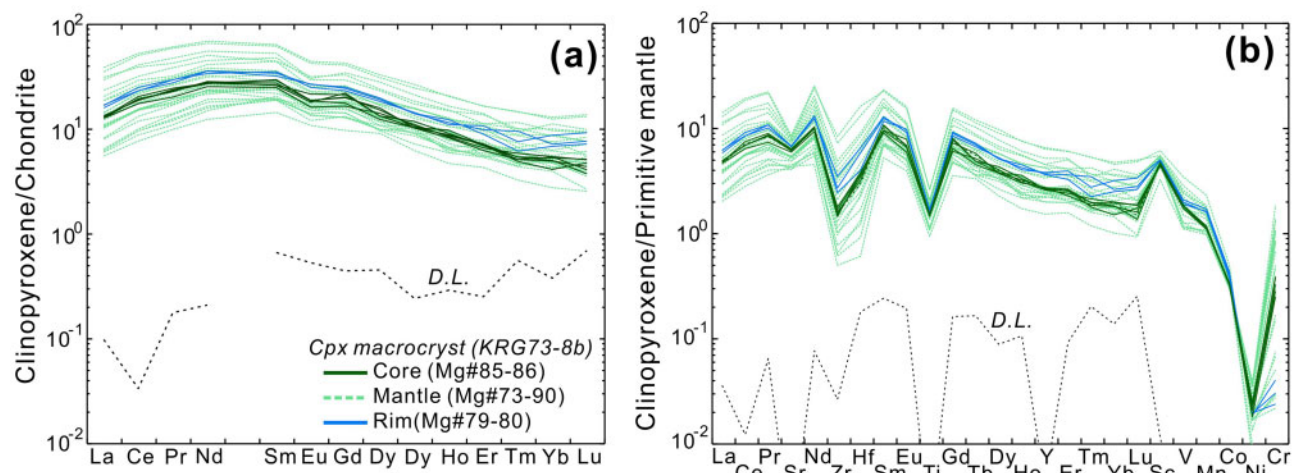

Fig. 7. Chondrite-normalized REE patterns (a) and primitive mantle-normalized trace element patterns (b) of a single Cpx macrocryst from the lamprophyre dyke. Chondrite and primitive mantle values are from McDonough & Sun (1995). D.L. denotes detection limit of LA-ICP-MS analysis.
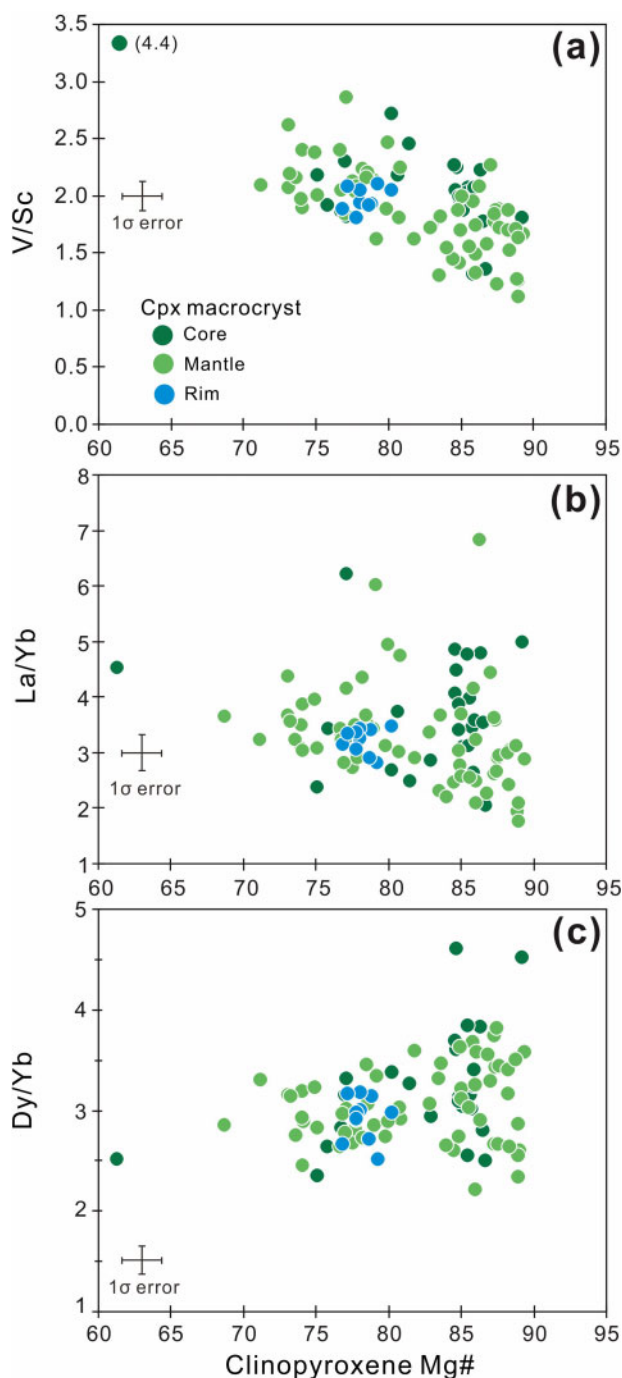
Fig. 8. Binary plots of Mg# vs V/Sc (a), La/Yb (b) and Dy/Yb (c) for the Cpx macrocrysts from the lamprophyre dyke.

concentric Cr-rich layers alternating with Cr-poor layers, whereas the closely packed layers with straight boundaries in the hourglass sector do not show clear Cr zoning (Fig. 10f).

Major and trace element profiles of Cpx macrocrysts

As the growth layers in a single Cpx macrocryst are usually asymmetric, the core-to-rim compositional profiles were deliberately acquired along the long axis so that we can obtain the compositions of as many layers as possible in each of the profiles (Figs 11 and 12). The profile of Mg# for a single crystal is remarkably different from one crystal to another. Most crystals have Mg# varying from 70 to 90 along the profiles (Supplementary Data Table S2).

A typical profile of the Cpx macrocrysts is composed of alternating coarse and fine layers, with the core having constantly high Mg# relative to the rim (Figs 11b and 12b). The mantle has high-amplitude oscillation of Mg#, Al_2O_3 and TiO_2 on the major resorption surfaces (R) and low-amplitude oscillation of Mg#, Al_2O_3 and TiO_2 between the closely packed layers. The Mg# of Cpx on R surfaces varies by *c*. ±6 to ±14 relative to neighboring layers (Figs 11b and 12b). In the closely packed layers with straight boundaries, the Mg# of Cpx varies by $<±2$ in the Si–Mg-rich sector and by *c*. ±2 to ±6 between the sector-zoned and concentric Cr-rich and Cr-poor layers (Fig. 13a and b). In the closely packed layers with wavy boundaries, the Mg# of Cpx varies by *c*. ±2 to ±4 at the boundaries (Fig. 13c and d). The Al_2O_3 and TiO_2 contents of the grain generally show opposite trends to Mg#; however, Al_2O_3 is overall less variable than TiO_2 within a single layer (Figs 11c and 12c). Overall, the profiles across different growth layers in the sector zoning of a macrocryst show clearly different compositional trends; the growth layers in the prism sector have similar compositions, whereas the growth layers in the hourglass sector have lower Al_2O_3 and TiO_2 and higher SiO_2 than those in the prism sector (Fig. 14a–c). Na_2O and MnO are only slightly enriched in the prism sector, and Cr_2O_3 and CaO are not obviously different between these sectors (Fig. 14d–f).

In a profile that is mainly composed of coarse layers (Fig. 15a), the core has relatively constant Mg# of ∼85, the mantle has four layers with Mg# of ∼85–90 alternating with five layers with Mg# of 71–76, and the rim has nearly constant Mg# of ∼79 (Fig. 15b). Al_2O_3 and TiO_2 have the opposite trend to Mg# in the profile (Fig. 15b). Chromium variation along the profile is consistent with Mg#, showing the highest Mg# with highest Cr concentration and vice versa (Fig. 15c). Strontium shows a trend opposite to that of Mg# and Cr along the profile (Fig. 15c). Both La/Yb and Dy/Yb along the profile do not vary systematically with Mg# (Fig. 15d and e). La/Yb along the profile varies from 1·8 to 4·8, whereas Dy/Yb varies from 2·3 to 3·7 (Supplementary Data Table S3).

Sr isotopic compositions of Cpx macrocrysts
Five Cpx macrocrysts have $^{87}Sr/^{86}Sr$ ranging from 0·7072 to 0·7084 (Supplementary Data Table S5), much lower than the whole-rock values (Fig. 16). It is also noted that either single grains or different grains within a single thin section have variable $^{87}Sr/^{86}Sr$. For instance, the domain with Mg# of 67–74 in Crystal 2 has $^{87}Sr/^{86}Sr$ of ∼0·7075, whereas the domain with similar Mg# in Crystal 3 has $^{87}Sr/^{86}Sr$ of ∼0·7094 (Fig. 16). Given that the laser beam adopted in this study is
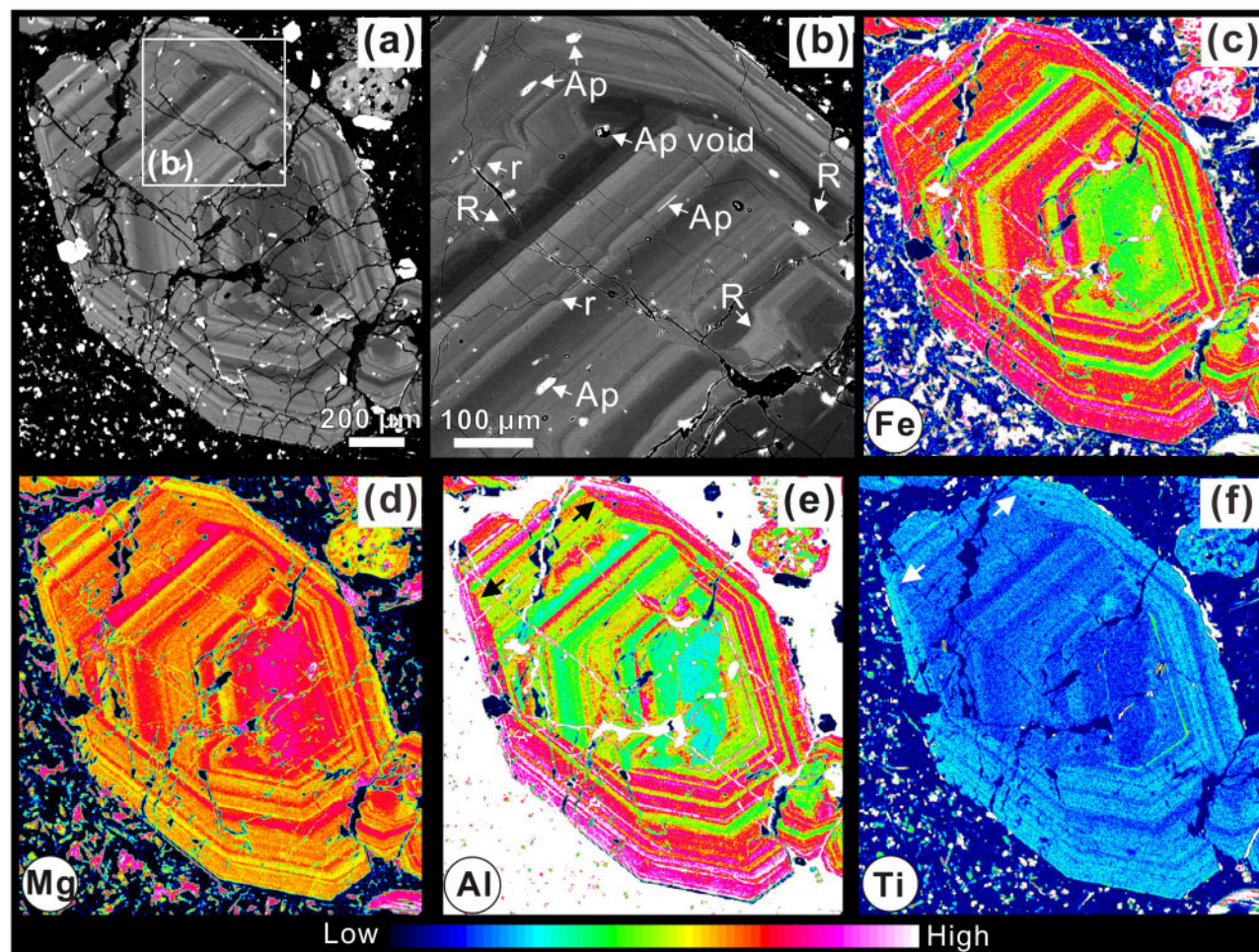
Fig. 9. Backscattered electron images (a, b) and EPMA elemental X-ray maps (c–f) of a Cpx macrocryst from the lamprophyre dyke. Noteworthy features are the remarkable oscillation of Fe, Mg, Al and Ti, and clear sector zoning in Al and Ti (marked by arrow).

155 μm, the results could be a mixture of coarse layers and many fine layers. However, the profile across the coarse layers of a macrocryst shows that the $^{87}Sr/^{86}Sr$ is constantly at 0·7078 in layers 1 and 3 despite Mg# varying from 85 to 74, and it decreases to 0·7073 in layer 4 with Mg# 86, and then keeps nearly constant at 0·7075–0·7076 from layer 6 to 11 despite Mg# varying from 76 to 89 (Fig. 15a).

DISCUSSION

Thermodynamic and kinetic effects on the growth of Cpx macrocrysts

The Cpx macrocrysts in this study are typically elongated with distinct oscillatory zoning, patchy zoning and sieve texture (Figs 3 and 4) and sector zoning (Figs 9 and 10), indicating that they may have experienced complex growth processes. Experimental studies demonstrate that the texture and composition of Cpx respond not only to thermodynamic conditions, but also to kinetic effects during crystal growth; for example, high degrees of undercooling or rapid decompression (Lofgren *et al.*, 2006; Mollo *et al.*, 2010, 2013;

Neave *et al.*, 2019; Pontesilli *et al.*, 2019; Masotta *et al.*, 2020). The complex textures and chemical compositions of the Cpx macrocrysts in this study may thus shed light on the thermodynamic conditions and kinetic effects of crustal magma reservoirs where the Cpx macrocrysts crystallized.

Oscillatory and sector zoning

Oscillatory zoning is common in plagioclase and clinopyroxene from terrestrial and lunar rocks, and has been substantially documented to decipher the role of crystallization kinetics as well as magma recharge events and convection processes (Downes, 1974; Eriksson, 1985; Clark *et al.*, 1986; O'Brien et al., 1988; Shimizu, 1990; Pearce 1994; Shore & Fowler 1996; Ginibre *et al.*, 2002a, 2002b; Humphreys *et al.*, 2006; Ginibre & Wörner, 2007; Streck, 2008; Elardo & Shearer, 2014). The oscillatory zoning of the Cpx macrocrysts in this study shows clear major and minor resorption surfaces between different layers, and high- or low-amplitude oscillation of Mg# and major and trace elements crosses layer boundaries (Figs 11, 12 and 15). Generally, overgrowth of a single layer with a clear
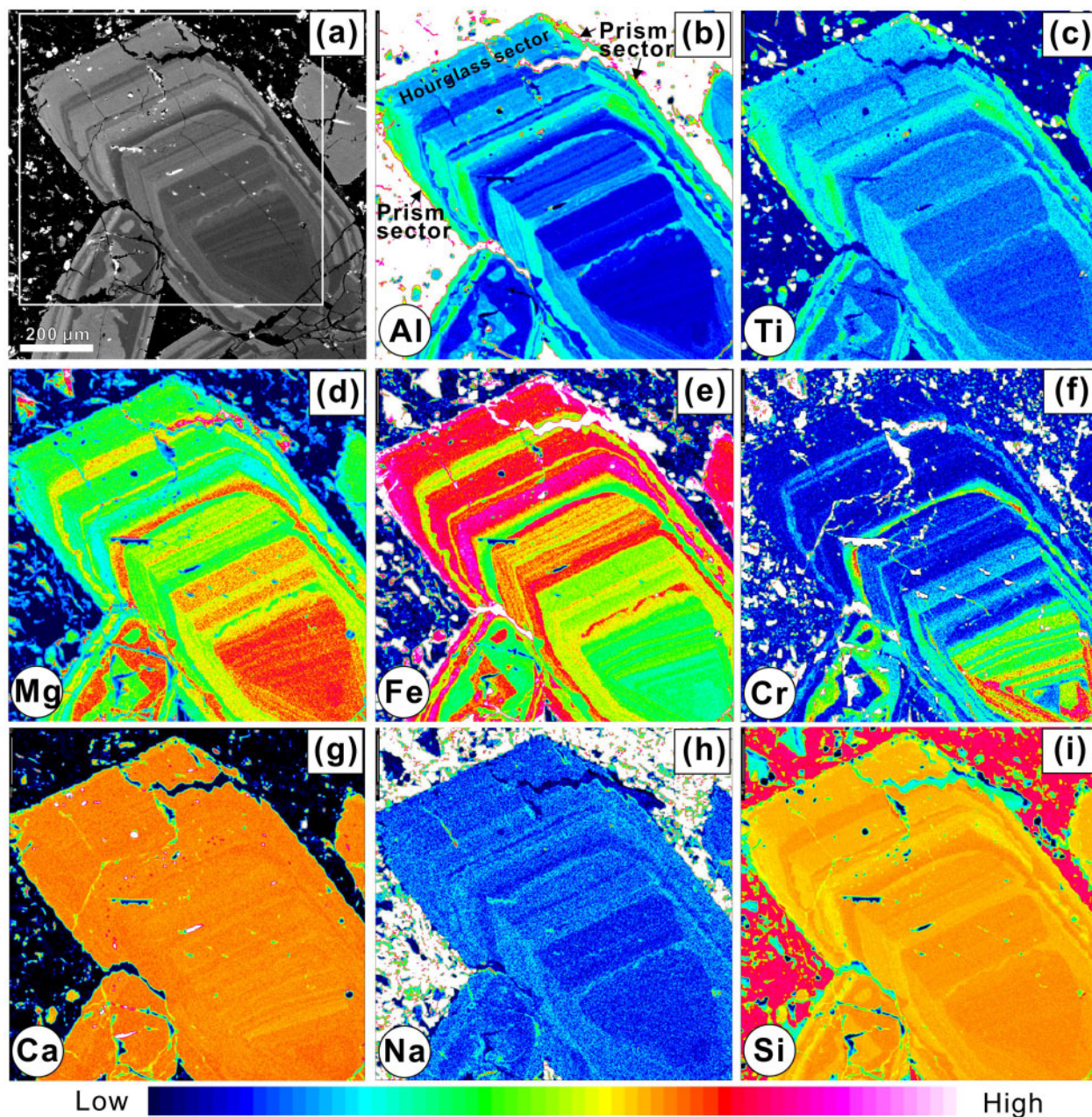
Fig. 10. Backscattered electron image (a) and EPMA elemental X-ray maps (b–i) of a Cpx macrocryst from the lamprophyre dyke. The element maps show distinct sector zoning that is not observed in the BSE image. The layers in the hourglass sector are enriched in Si and Mg, whereas the layers in the prism sector are enriched in Al and Ti. Na is weakly enriched in the prism sector. In contrast, Cr and Fe maps show concentric zoning. Ca map shows slight differences in the crystal. It is noteworthy that the closely packed layers with straight boundaries are distributed in the Si–Mg-rich sector, whereas the closely packed layers with wavy boundaries show concentric Cr-rich layers alternating with Cr-poor layers.

resorption surface is attributed to a change of melt composition during crystallization of a crystal (Ginibre *et al.*, 2002a, 2002b); a major resorption surface with high-amplitude oscillation of major elements may indicate a major magma recharge event of compositionally different magma, whereas a minor resorption surface with low-amplitude oscillation of major elements may be produced by the mixing of magmas with less contrasting compositions locally (Ginibre & Wörner, 2007; Elardo & Shearer, 2014). Therefore, the resorption

surfaces in the Cpx macrocrysts are assumed to respond to variable degrees of magma mixing. The major and minor resorption surfaces in the profile of Fig. 15 are associated with either high Mg# and high Cr or low Mg# and low Cr oscillations (Fig. 15a–c), indicating multiple recharging events involving primary or evolved magmas during the growth of a crystal.

Clear Si- and Mg-rich hourglass sectors and Al- and Ti-rich prism sectors in the macrocryst (Fig. 14) are similar to the sector zoning of augite in the lavas of Mt Etna
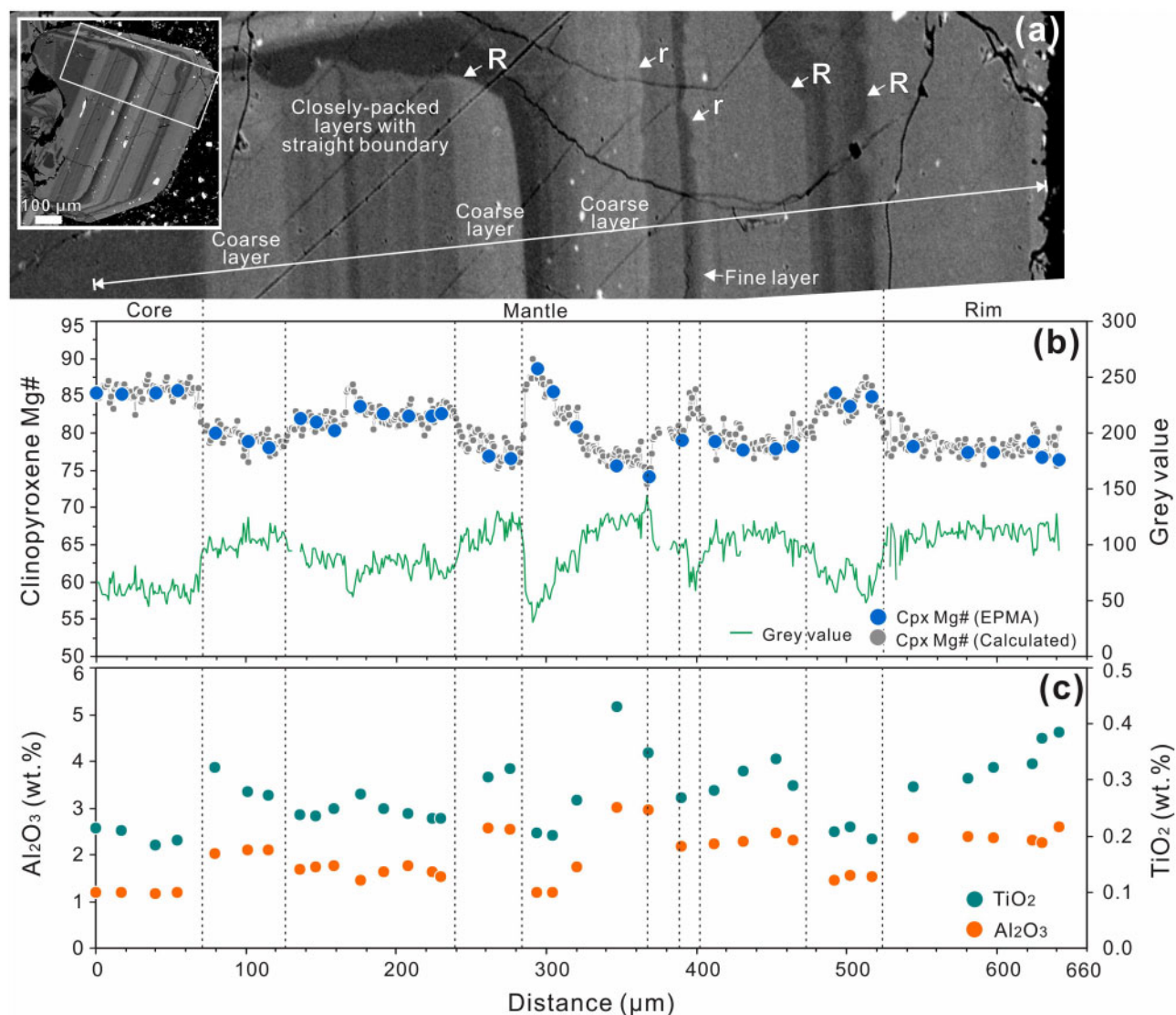
Fig. 11. Backscattered electron image (a) and compositional profiles (b, c) across a Cpx macrocryst from the lamprophyre dyke. (a) The grain contains multiple zoning patterns, including alternating coarse and fine layers and closely packed layers with straight boundaries. It should be noted that the major (R) and minor (r) resorption surfaces are well developed. (b) Mg# profile obtained by EPMA and conversion by grey-value regression along the white line marked in (a). (c) Profiles of Al_2O_3 and TiO_2 contents obtained by EPMA.

in Italy (Ubide *et al.*, 2019*a*) and Holuhraun in Iceland (Neave *et al.*, 2019), and are also similar to those of experimental Cpx resulting from alkaline melts (Masotta *et al.*, 2020). The compositional difference between the hourglass and prism sectors can be attributed to cation exchange of $[Si^{4+} + Mg^{2+}]_{hourglass} \iff [Ti^{4+} + Al^{3+}]_{prism}$ or $[Si^{4+} + Fe^{2+} + Mg^{2+}]_{hourglass} \iff [Ti^{4+} + Al^{3+} + Fe^{3+} + Ca^{2+} + Na^+]_{prism}$ at low degrees of undercooling or under near-equilibrium conditions, and could be an effective indicator of sluggish kinetic effect (Neave *et al.*, 2019; Ubide *et al.*, 2019*a*; Masotta *et al.*, 2020). Therefore, the sector zoning of Cpx with compositions similar to those formed at low degrees of undercooling can be used to reconstruct the magma plumbing and storage system (Neave *et al.*, 2019; Ubide *et al.*, 2019*a*, 2019*b*).

The closely packed layers in the Cpx macrocrysts show high-frequency, low-amplitude oscillation of Mg# (Fig. 13), similar to those in the plagioclase phenocrysts from dacite of the Parinacota volcano in Chile (Ginibre *et al.*, 2002*a*). The closely packed layers with straight boundaries actually consist of concentric Cr-rich and Cr-poor layers and multiple fine layers in the Si–Mg-rich sector (Fig. 13a), indicating that the crystallization kinetics was disrupted frequently by magma recharging events. On the other hand, the wavy boundaries of closely packed layers (Fig. 13c) indicate frequent, small-scale resorption, which could be developed by rapid movement of crystals under large thermal and chemical gradients by magma convection (Ginibre *et al.*, 2002*a*, 2002*b*; Ginibre & Wörner, 2007). The rapid movement of crystals through thermal and chemical gradients can
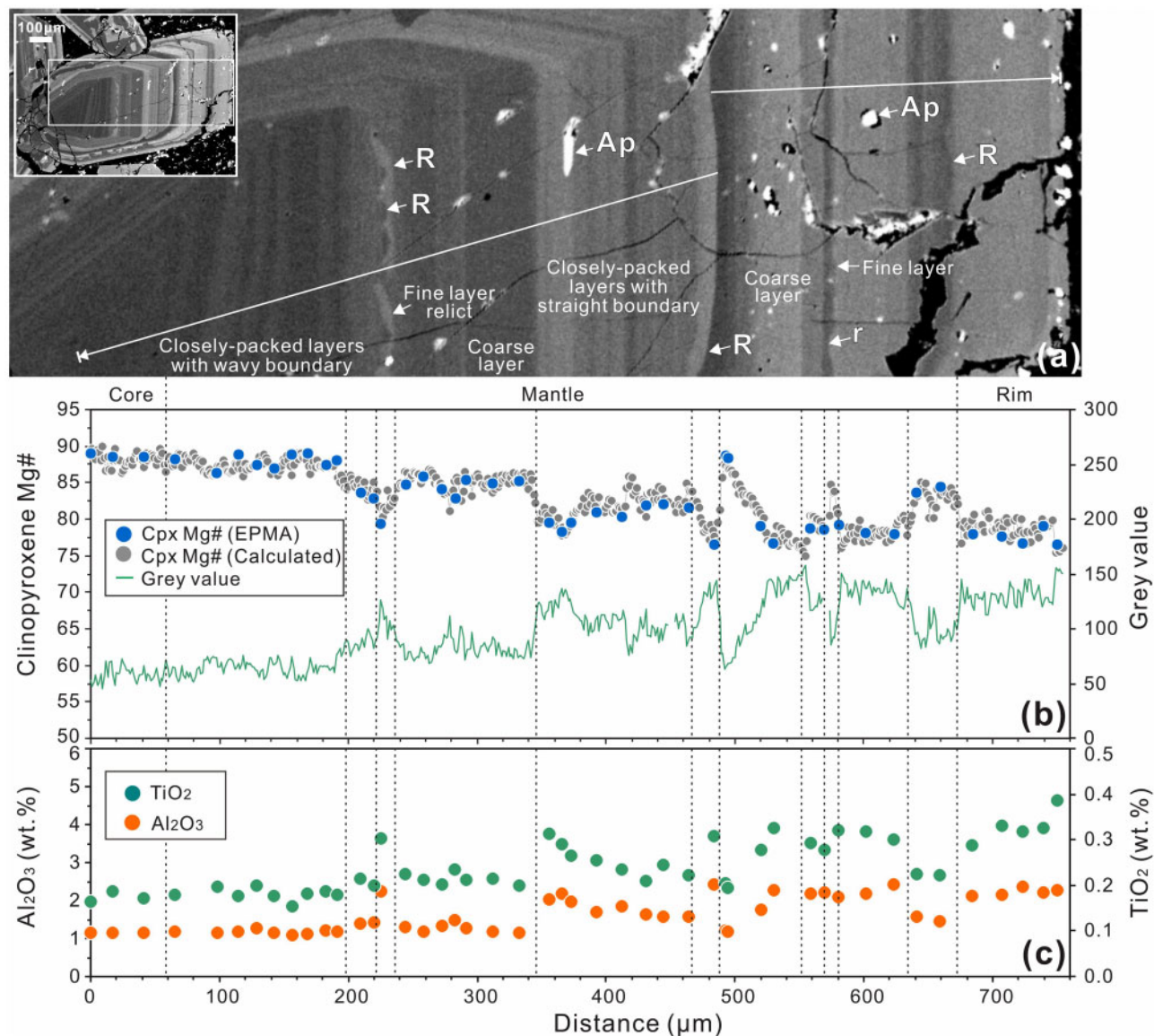
Fig. 12. Backscattered electron image (a) and compositional profiles (b, c) across a Cpx microcryst from the lamprophyre dyke. (a) The grain shows alternating coarse and fine layers, closely packed layers with wavy boundaries and straight boundaries. It should be noted that major (R) and minor (r) resorption surfaces are developed. (b) Mg# profile obtained by EPMA results and conversion by grey-value regression along the white line marked in (a). (c) Profiles of Al_2O_3 and TiO_2 contents obtained by EPMA.

frequently change the composition and temperature of the ambient melts surrounding the crystals. Only fine layers may be developed because the retention of crystals was time-limited in this situation (Singer *et al.*, 1995; Ginibre *et al.*, 2002a).

Patchy zoning and sieve texture
The patchy zoning indicates intense dissolution of early crystallized Cpx by recharged, relatively primary magma, as evidenced by the presence of abundant melt inclusions in the high-Mg#, dark domains of the patchy zoning (Fig. 4a). The sieve texture is commonly associated with patchy zoning in the cores of the Cpx macrocrysts, and abundant mica and matrix fill the spongy space of the sieve texture (Fig. 4b and c). Sieve

texture is common in the plagioclase and pyroxene of volcanic rocks and mantle xenoliths, and can be developed as a result of changes in temperature, pressure or melt compositions (O'Brien et al., 1988; Nelson & Montana, 1992; Stewart & Pearce, 2004; Tomiya & Takahashi, 2005; Humphreys *et al.*, 2006; Pan *et al.*, 2018). High degrees of undercooling could lead to rapid skeletal growth of Cpx with spongy space filled with matrix, leaving distinct skeletal or dendritic zoning with regular fine layers in the crystal (Masotta *et al.*, 2020). This, however, is not observed in the sieve texture of the Cpx macrocrysts in this study. Rapid decompression during fast ascent of magmas could result in coarse-scale sieve texture and higher Mg# and lower Al_2O_3 of clinopyroxene than those of the primary crystals in mantle xenoliths (Pan *et al.*, 2018). The
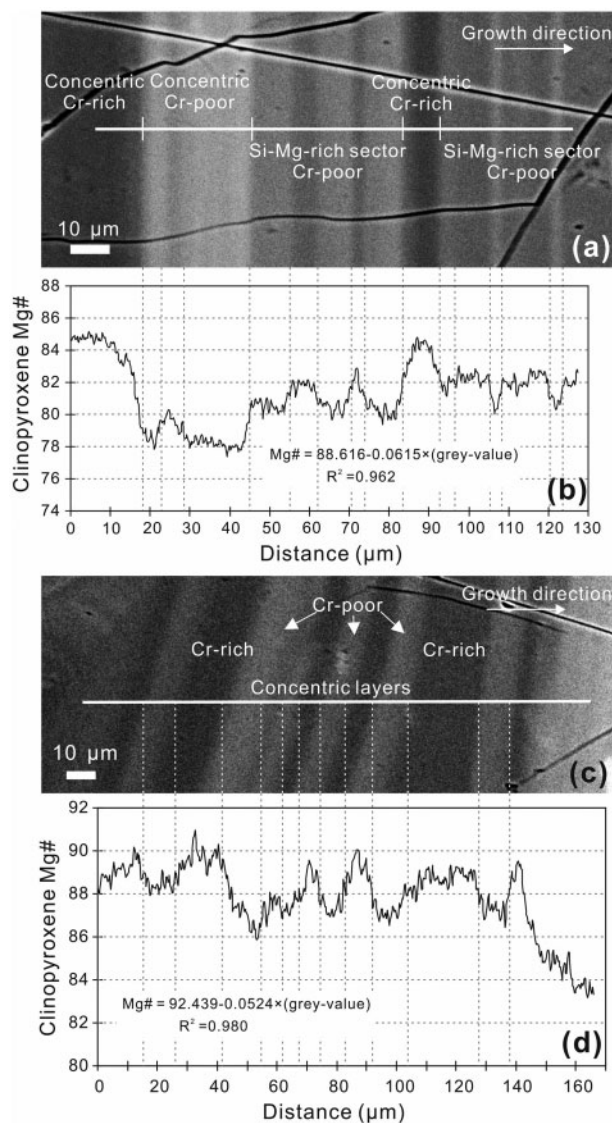
Fig. 13. Backscattered electron images (a, c) and profiles of Cpx Mg# converted by grey-value regression across the closely packed layers (b, d). Both the closely packed layers with straight boundaries (a) and with wavy boundaries (c) show high-frequency oscillation of Mg#. It should be noted that the closely packed layers in the Si–Mg-rich sector show low-amplitude oscillation of Mg# ($< \pm 2$) at the layer boundaries (b). The boundaries between the closely packed layers and the concentric Cr-rich/Cr-poor layers have Mg# varying by ± 2 to ± 6 (b). The closely packed layers with wavy boundaries show ± 2 to ± 4 variation of Mg# at the layer boundaries (d).

decompression-driven dissolution and reprecipitation of Cpx in volcanic rocks also lowers Al_2O_3 in the rim (Neave & Maclennan, 2020). However, the sieved cores of the Cpx macrocrysts in this study have similar Mg# range and high Al_2O_3 relative to the mantles and rims (Figs 4c, d and 6c); they are thus unlikely to have formed owing to rapid decompression. Instead, the sieved cores may be attributed to the dissolution of Cpx by groundmass melt. The cracks functioned as channels that allowed the groundmass melt to penetrate and partially resorb the cores, leading locally to chemical

disequilibrium of the ambient melt. The re-precipitation of the ambient melt may cause the compositions of the sieved cores to significantly deviate from the trends of the cores and mantles of the Cpx macrocrysts (Fig. 6).

It is also noted that the concentric layers developed in some Cpx glomerocrysts with sieve texture can be traced among the grains without obvious resorption (Fig. 4e), indicating that these grains grew simultaneously and the sieve texture formed during crystal growth rather than late-stage dissolution. The radiating growth of multiple crystals is probably attributed to heterogeneous nucleation of crystals at high degrees of undercooling (see Shea & Hammer, 2013). Therefore, the sieve texture of the Cpx macrocrysts in this study formed either by late-stage dissolution and re-precipitation of the groundmass melt or by high degrees of undercooling, such Cpx macrocrystsare not applicable to reconstruct the magma plumbing and storage system.

Multi-mantle sources for the lamprophyre dyke

The complex oscillatory zoning patterns and highly variable compositions of the cores and mantles of the Cpx macrocrysts in this study (Figs 5 and 6) indicate that the host lamprophyre dyke may contain diverse crystal populations, which may be either from multiple batches of magmas that share the same mantle source or from magmas derived from different mantle sources (Humphreys et al., 2006; Winpenny & Maclennan, 2011; Neave et al., 2013, 2014; Ubide et al., 2014).

Experimental results reveal that the ratios of partition coefficients of REE between Cpx and melt would not change dramatically on cooling, even at high cooling rates (Lofgren et al., 2006; Mollo et al., 2013). For example, the partition coefficient ratios of La/Yb and Dy/Yb between Cpx and trachybasaltic melt increase by only ~ 0.08 when the cooling rate increases from $2\,°C\,h^{-1}$ to $50\,°C\,h^{-1}$ (Mollo et al., 2013). Therefore, the REE partition coefficient ratios of Cpx are considered to be nearly constant despite high degrees of undercooling (Winpenny & Maclennan, 2011) or fractionation of basaltic magma (Lissenberg & MacLeod, 2016). The La/Yb and Dy/Yb ratios of ultrapotassic rocks and the melt in equilibrium with clinopyroxene have been widely applied to distinguish their mantle sources and melting process (Miller et al., 1999; Duggen et al., 2005; Prelević et al., 2012). We thus use La/Yb and Dy/Yb of the Cpx macrocrysts to constrain the mantle melting processes of the lamprophyre dyke in this study.

The Cpx macrocrysts have $^{87}Sr/^{86}Sr$ much lower than those of the host lamprophyre dyke (Fig. 16), indicating significant crustal contamination during magma ascent or late-stage fluid alteration. As the Cpx macrocrysts are relatively fresh and show distinct major and trace element zoning (Figs 11, 12 and 15), fluid alteration should have only a trivial effect on these macrocrysts. To avoid the possible effects of crustal contamination and REE fractionation caused by
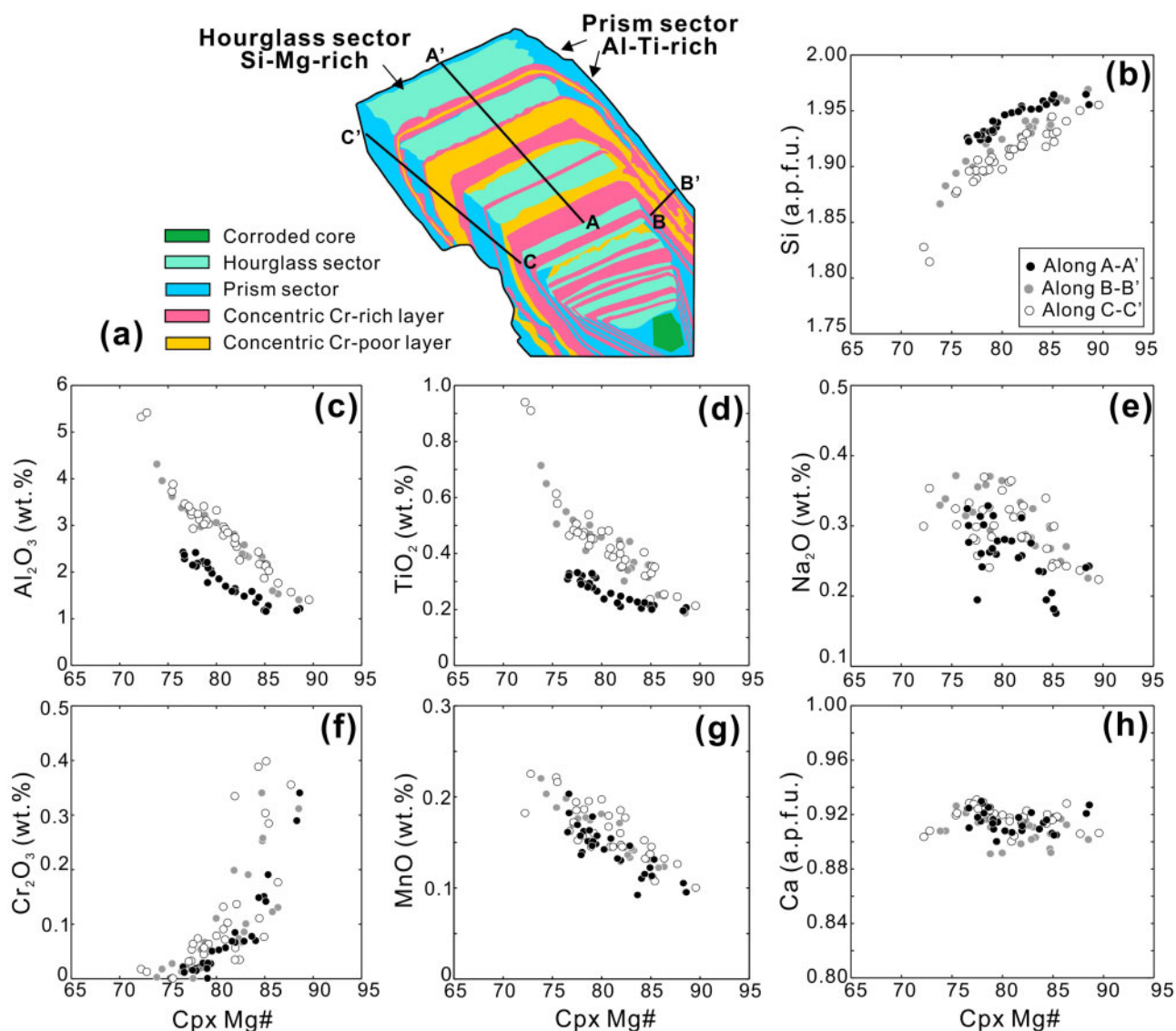
Fig. 14. A sketch of the Cpx macrocryst observed in the 2-D elemental maps in Fig. 10 and binary plots of Mg# vs major and minor elements contents obtained by EPMA (b–h).

fractional crystallization in the crustal magma reservoirs, only the domains with high Mg# ($\geq$85) were chosen to calculate the compositions of equilibrium melts using the equation $C_i^{Melt} = C_i^{Cpx}/D_i^{Cpx/Melt}$, where C_i^{Melt} and C_i^{Cpx} refer to the concentration of element i in melt and clinopyroxene, respectively, and $D_i^{Cpx/Melt}$ refers to the partition coefficient of i between clinopyroxene and melt. The $D_{La}^{Cpx/Melt}$, $D_{Dy}^{Cpx/Melt}$ and $D_{Yb}^{Cpx/Melt}$ values used in this study are 0·029, 0·33 and 0·22, respectively (after Prelević *et al.*, 2012). The equilibrium melts were calculated to have La/Yb varying from 13·6 to 37·9 and Dy/Yb from 1·56 to 3·02 (Fig. 17a), and have scattered La/Yb against variable Yb concentration (Fig. 17b), indicating that they were probably derived from multiple mantle sources.

It is generally acknowledged that melting of a four-phase peridotite mantle cannot produce ultrapotassic

melts and thus a K-rich phase (phlogopite) is required in the mantle source (Foley, 1992*a*). A vein plus wall-rock melting model was proposed to explain the generation of potassic–ultapotassic melt (Foley, 1992*b*); however, the melting process is difficult to model quantitatively because of the variability in the mineralogy, mineral modes and chemical compositions of the mantle (Miller *et al.*, 1999). Nonetheless, Group III ultra-potassic rocks in orogeny are considered to have originated from relatively fertile spinel-peridotite mantle with abundant clinopyroxene and mica (Foley, 1992*a*). They may also have been derived from a deeper garnet-peridotite source as the rocks and the Cpx commonly have more depleted HREE than LREE (Miller *et al.*, 1999; Prelević *et al.*, 2012; Gülmez *et al.*, 2016). To simulate the contribution of garnet- or spinel-field mantle sources to the lamprophyre dyke in this study, we carried
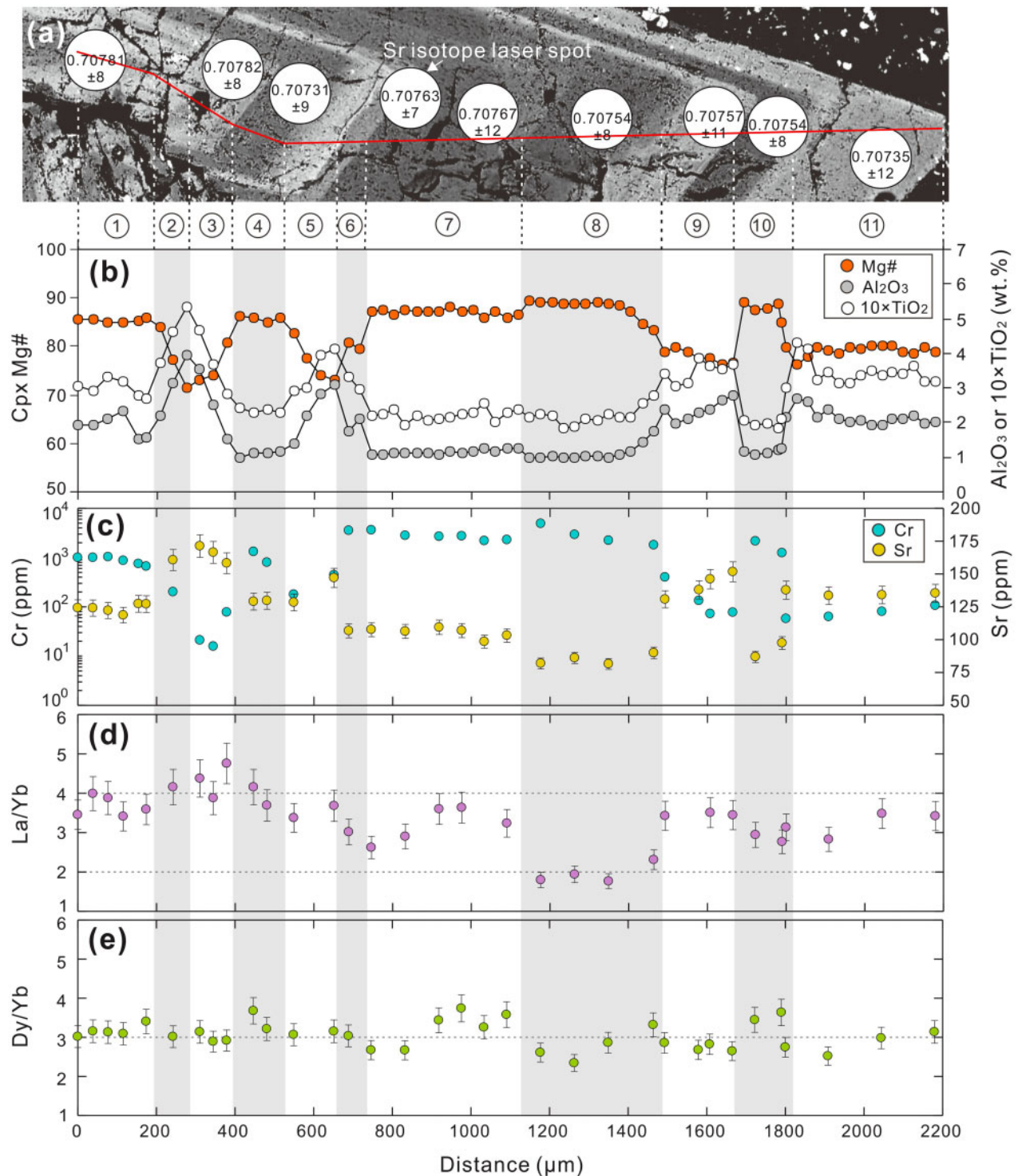
Fig. 15. Backscattered electron image (a) and compositional profiles of major and trace elements (b–e) for a Cpx macrocryst mainly consisting of coarse layers (the crystal on the left in Fig. 3a). (b) Profiles of Mg#, Al_2O_3 and TiO_2 contents obtained by EPMA. (c–e) Profiles of Cr, Sr, La/Yb and Dy/Yb obtained by LA-ICP-MS. Sr isotope compositions obtained by LA-MC-ICP-MS are marked in (a).

out a modelling study based on a non-modal, fractional partial melting model (see Shaw, 1970).

Phlogopite harzburgite was generally considered to be the mantle source of lamproite (Foley, 1992a; Prelević et al., 2012). However, modelling for the phlogopite harzburgite using the partial melting curves

of Prelević et al. (2012) would obtain high Dy/Yb, and it may require nearly 40 % partial melting to explain the variations of La/Yb of the equilibrium melts in this study (Fig. 17a).

We adopted phlogopite lherzolite in the modelling of this study, which was also used in the partial melting
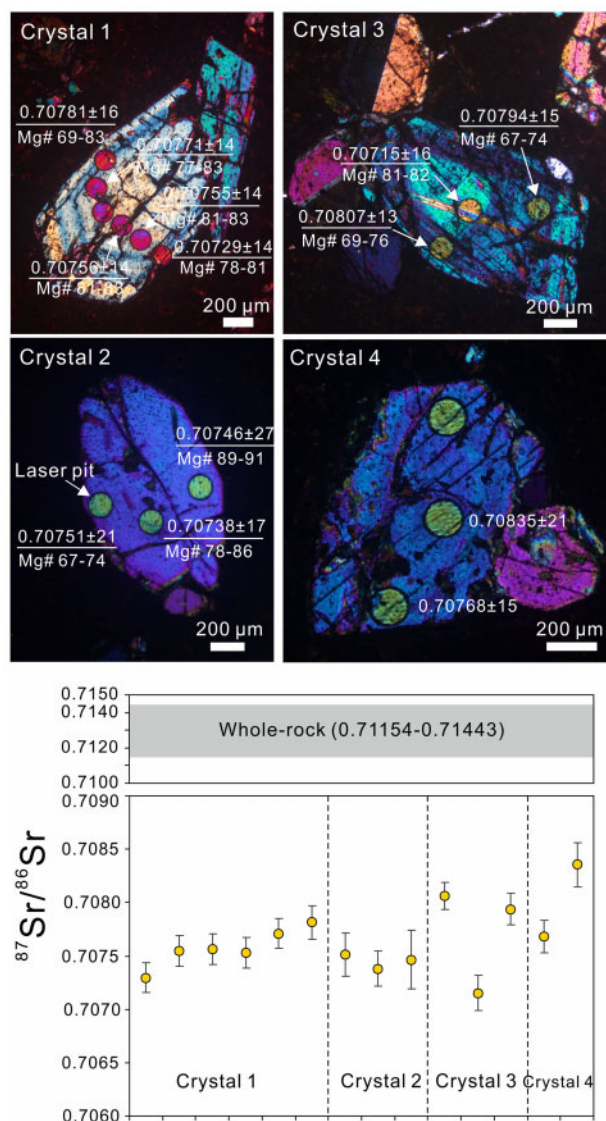
Fig. 16. *In situ* Sr isotopes of the Cpx macrocrysts from the lamprophyre dyke. It should be noted that the whole-rocks have higher $^{87}Sr/^{86}Sr$ ratios than those of the Cpx macrocrysts.

modelling for potassic and ultrapotassic rocks in the westernmost Mediterranean (Duggen *et al*., 2005). The CI chondrite values of Sun & McDonough (1989) were adopted as the initial compositions of the garnet/spinel lherzolite mantle. The median values of the metasomatized subcontinental lithospheric mantle of McDonough (1990) were adopted as the initial compositions of garnet/spinel phlogopite lherzolite mantle. The results indicate that the melts in equilibrium with Cpx of Mg# ≥85 have La/Yb and Dy/Yb deviating from any of the modelled melting curves of mantle sources (Fig. 17), arguing that magmas of the lamprophyre dyke may have been derived from different mantle sources.

The modelling results of magma mixing show that the La/Yb and Dy/Yb of the equilibrium melts could be simulated by the melts produced by 1–5 % melting of the garnet phlogopite lherzolite mixed with the melts
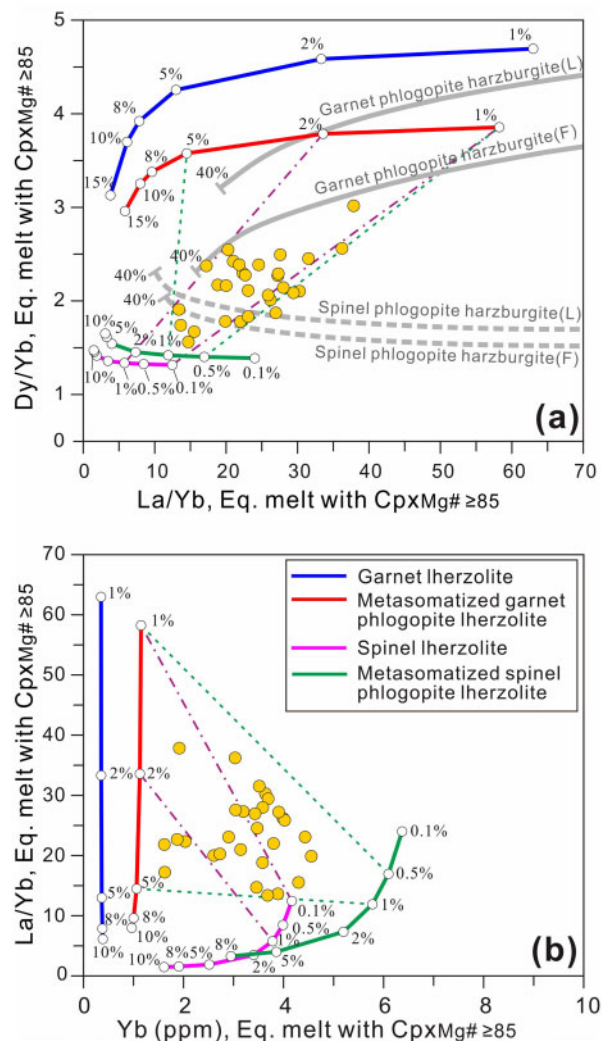

Fig. 17. Binary plots of calculated La/Yb vs Dy/Yb (a) and Yb vs Dy/Yb (b) of melts in equilibrium with high-Mg# (≥85) Cpx domains. The melt compositions in equilibrium with Cpx were calculated using partition coefficients of $D_{La,Dy,Yb}^{Cpx-melt} = 0.029$, 0.33 and 0.22 (Prelević *et al*., 2012). Non-modal, fractional partial melting was modelled for garnet lherzolite ($Ol_{0.598}Opx_{0.211}Cpx_{0.076}Grt_{0.115}$), spinel lherzolite ($Ol_{0.578}Opx_{0.270}Cpx_{0.119}Sp_{0.033}$) and metasomatized garnet phlogopite lherzolite ($Ol_{0.564}Opx_{0.188}Cpx_{0.141}Grt_{0.047}Phl_{0.06}$) and metasomatized spinel phlogopite lherzolite ($Ol_{0.564}Opx_{0.188}Cpx_{0.141}Sp_{0.024}Phl_{0.083}$). Source compositions of La, Dy and Yb are assumed to be 0.237, 0.254 and 0.17 ppm (CI chondritic REE composition; Sun & McDonough, 1989) for garnet/spinel lherzolite and 0.77, 0.47 and 0.27 ppm (median values of metasomatized lithosphere mantle; McDonough, 1990) for metasomatized garnet/spinel phlogopite lherzolite. Phase proportions entering the partial melt are taken as $Ol_{0.05}Opx_{0.2}Cpx_{0.3}Grt_{0.45}$ for garnet lherzolite, $Ol_{0.1}Opx_{0.27}Cpx_{0.5}Sp_{0.13}$ for spinel lherzolite, $Ol_{0.1}Opx_{0.15}Cpx_{0.3}Grt_{0.1}Phl_{0.35}$ for garnet phlogopite lherzolite, and $Ol_{0.1}Opx_{0.15}Cpx_{0.3}Sp_{0.05}Phl_{0.4}$ for spinel phlogopite lherzolite, respectively. Partition coefficients used in modelling are $D_{La,Dy,Yb}^{Ol-melt} = 0$, 0.007, 0.0011, $D_{La,Dy,Yb}^{Opx-melt} = 0.002$, 0.022, 0.049, $D_{La,Dy,Yb}^{Grt-melt} = 0.01$, 1.06, 4.01, $D_{La,Dy,Yb}^{Sp-melt} = 0.002$, 0.01, 0.01, $D_{La,Dy,Yb}^{Phl-melt} = 0.0001$, 0.017, 0.01, which are adopted from McKenzie & O'Nions (1991), Duggen *et al*. (2005) and Prelević *et al*. (2012). Melting curves of metasomatized garnet/spinel phlogopite harzburgite with source compositions of metasomatized continental lithospheric (L) mantle and Finero (F) phlogopite harzburgite were adopted from Prelević *et al*. (2012).

produced by 0·5–1% melting of the spinel phlogopite lherzolite, or the melts by 1–2% melting of the garnet phlogopite lherzolite mixed with the melts by 0·1–1% melting of the spinel lherzolite (Fig. 17). It is thus likely that magmas of the lamprophyre dyke may have been derived from different mantle sources with either enriched or depleted nature; the high-Mg# (∼85) domains with high La/Yb in the Cpx macrocrysts may represent the crystallization products of the enriched melts, whereas those high-Mg# (∼90) domains with low La/Yb may represent the crystallization products of the depleted melts (Fig. 8b).

Estimation for the depths of crustal magma reservoirs

Thermobarometers based on Cpx–melt compositions can be used to estimate the crystallization pressure of Cpx in volcanic rocks (Putirka *et al.*, 1996, 2003; Putirka, 2008), inferring the depth of crustal magma reservoirs. We chose the Cpx–melt thermometer [equation T1 of Putirka *et al.* (1996)] and the Cpx–melt barometer [equation A of Putirka *et al.* (2003)] to estimate the crystallization temperature and pressure of the Cpx macrocrysts in this study. The Cpx–melt thermobarometer could give comparable results for the crystallization pressures of hourglass and prism sectors so that the kinetic effect on the compositions of Cpx could be eliminated (Neave *et al.*, 2019; Ubide *et al.*, 2019*a*). The thermobarometer we used in this study yields one standard error of estimate (1SEE) of ±27 °C and ±1·3 kbar, respectively (Putirka *et al.*, 1996, 2003).

Because the rocks from the lamprophyre dyke have restricted major element contents and higher $^{87}Sr/^{86}Sr$ than that of the Cpx macrocrysts, the whole-rock compositions cannot represent the equilibrium melts. The equilibrium melts of the Cpx macrocrysts in this study were selected by matching compositions from a large dataset ($n = 2951$) of potassic–ultrapotassic rocks in the literature and lamprophyre and lamproite in the GEOROC database (http://georoc.mpch-mainz.gwdg.de/georoc/), following the procedures of Neave *et al.* (2013, 2019) and Ubide *et al.* (2019*b*). To effectively identify the Cpx–melt equilibrium, we compared the components of diopside + hedenbergite (DiHd) and enstatite + ferrosilite (EnFs) between those analyzed in Cpx and those predicted for Cpx–melt pairs (Mollo *et al.*, 2013). We also compared the measured and predicted partition coefficients of Na [D_{Na}; equation 7 of Blundy *et al.* (1995)] and Ti [D_{Ti}; equation 44 of Wood & Blundy (2003)], and Fe–Mg exchange coefficient between Cpx and melt [$Kd_{Fe-Mg}^{Cpx-melt}$; equation 35 of Putirka (2008)] as additional tests for the Cpx–melt pairs. Therefore, we carried out five tests to check the equilibration of each Cpx–melt pair, including DiHd, EnFs, D_{Na}, D_{Ti} and Kd_{Fe-Mg}. The thresholds used for $\Delta DiHd$, $\Delta EnFs$, ΔD_{Na} and ΔKd_{Fe-Mg} were ±0·06, ±0·05, ±0·02, and ±0·08, respectively, which are the same as the 1SEE of predicted values (Blundy *et al.*, 1995; Putirka, 2008; Mollo *et al.*, 2013).

The threshold used for ΔD_{Ti} was set to be ±0·2. As the Cpx–melt thermobarometer is sensitive to the jadeite (Jd) component of Cpx and Na_2O content of the equilibrium melt (Putirka *et al.*, 1996, 2003), the EPMA results for the core and rim of the Cpx macrocrysts were carefully checked to preclude the points with variation of Jd (ΔJd) larger than 0·003. In addition, the variation of predicted D_{Na} for each core and rim was restrained to be ≤0·02, which can effectively remove abnormal pressure values. With these filters, a number of equilibrium melts were matched with Cpx from the dataset.

A total of 123 Cpx–melt pairs were finally matched within the thresholds of predicted values (Fig. 18 and Supplementary Data Table S6). The Cpx in these pairs has Mg# varying from 76 to 87 and one standard deviation of estimated temperature and pressure are smaller than the model errors (Fig. 19a). The obtained pressure values for the cores vary from 1·5 to 5·8 kbar, and can be clearly distinguished into three populations (i.e. ∼5·4, ∼3·3 and ∼1·5 kbar, respectively; Fig. 19b), indicating that they may come from magma reservoirs at different depths. In contrast, the obtained pressure values for the rims are restricted from 1 to 2 kbar with an average of ∼1·6 kbar (Fig. 19b). We therefore consider that there were probably magma reservoirs of ultrapotassic magmas at three different depths equivalent to the crystallization pressures of ∼5·4, ∼3·3 and ∼1·6 kbar, respectively, making up a transcrustal magmatic system.

For the cores of the Cpx macrocrysts with low Mg# (<70), the equilibrium melts were selected by matching compositions from trachyandesite ($n = 4470$) and basaltic andesite and andesite ($n = 1995$) in the GEOROC and PetDB database (www.earthchem.org/petdb). A total of 45 Cpx–melt pairs were obtained within the same thresholds of predicted and measured values (Supplementary Data Table S6). The Cpx in these pairs has Mg# varying from 61 to 64 and the crystallization pressure is estimated to be ∼2·9–3·5 kbar (Fig. 19a). Therefore, the low-Mg# (<70) cores of the Cpx macrocrysts could be xenocrysts that were probably entrapped by the ultrapotassic magmas during magma upwelling. This can explain the distinct gap of Mg# between Core II and Core III (Fig. 5a).

The high-Mg# (≥88) domains have the highest Cr and lowest La/Yb among the Cpx macrocrysts (Fig. 8b), and no equilibrium melts can be matched for them from the dataset used in this study. These high-Mg# (≥88) domains may have crystallized early from primary, depleted magmas, which may be stored in the magma reservoir somewhere deeper in the crust or replenished directly into the shallower reservoirs, forming high-Mg# core and mantle of the Cpx macrocrysts.

A petrological model for the formation of the ultrapotassic dyke

The complex zoning patterns and compositions of the Cpx macrocrysts in the lamprophyre dyke could be
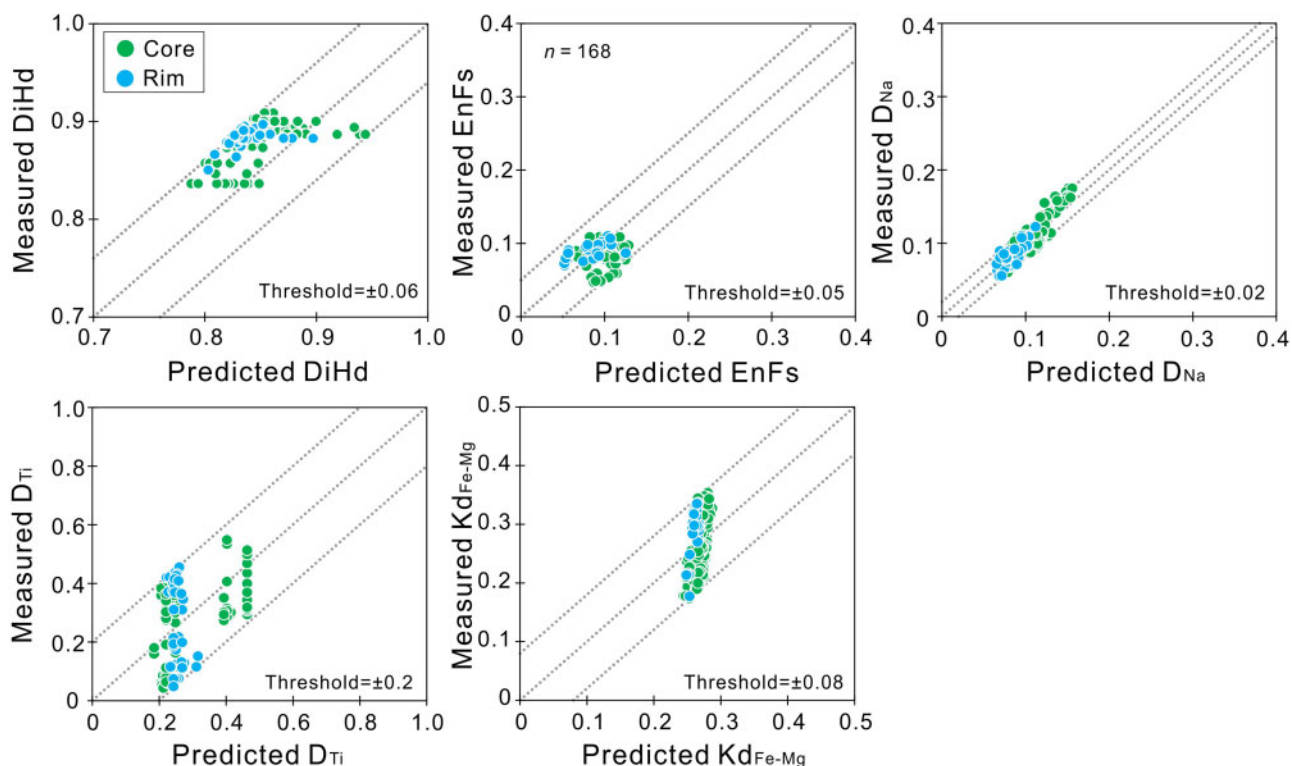
Fig. 18. Results of Cpx–melt equilibrium pairs selected by matching compositions of the cores and rims of the Cpx macrocrysts and a large dataset downloaded from the GEOROC database (http://georoc.mpch-mainz.gwdg.de/georoc/) and the PetDB database (www.earthchem.org/petdb). Five tests were used to check if the equilibrium is achieved: DiHd and EnFs (Mollo *et al.*, 2013), D_{Na} (Blundy *et al.*, 1995), D_{Ti} (Wood & Blundy, 2003) and Kd_{Fe-Mg} (Putirka, 2008). The thresholds between the predicted values and measured values for ΔDiHd, ΔEnFs, ΔD_{Na}, ΔD_{Ti} and ΔKd_{Fe-Mg} were ±0.06, ±0.05, ±0.02, ±0.2 and ±0.08, respectively (see details in the text).

developed in a magmatic system in the middle to upper crust. Distinct populations of the Cpx macrocrysts may have crystallized from multiple batches of magmas, which were supplied from different magma reservoirs in the system (Fig. 20a). The domains that have similar Mg# and different $^{87}Sr/^{86}Sr$ in different Cpx macrocrysts (Fig. 16) may have crystallized from different magma reservoirs. The similar Mg# range of the cores and mantles of the Cpx macrocrysts (Fig. 5a and b) is attributed to progressive replenishment of Cpx-laden magmas from different deep-seated magma reservoirs into shallow magma reservoirs where ultrapotassic magmas eventually developed.

The major magma reservoirs in the system may occur at three different depths in the middle to upper crust (i.e. ~5.4, ~3.3 and ~1.6 kbar, respectively), on the basis of estimated crystallization pressures of the Cpx macrocrysts (Fig. 20a). The primary, enriched magmas were probably produced by partial melting of the metasomatized garnet/spinel phlogopite lherzolite mantle, and they may replenish both the deep and shallow magma reservoirs, forming high-Mg# (85–87) Cpx domains with high La/Yb. Fractional crystallization of the primary, enriched magmas in the deeper reservoirs resulted in the evolved magmas, which may have

further frequently replenished the shallower reservoirs and crystallized low-Mg# (84–70) Cpx domains with high La/Yb. The primary, depleted magmas were probably produced by partial melting of the spinel-facies lherzolite mantle, and they may have crystallized high-Mg# (88–90) Cpx domains with low La/Yb in either deeper or shallower magma reservoirs. Mixing of the depleted and enriched magmas may have occurred in the shallower reservoir, resulting in the domain with variable Mg# and La/Yb. In addition, the clinopyroxene population with low Mg# (~64) and high La/Yb may have crystallized from an andesitic magma reservoir and become entrapped by the enriched magmas during ascent (Fig. 20a).

Concurrent mixing and crystallization in the magma reservoirs produced crystal-rich mush. The shallower magma reservoir was probably progressively recharged with the crystal-rich mush from deeper magma reservoirs. The Cpx grains that crystallized from the same or different magma batches may have accumulated together, forming Cpx glomerocrysts that show either similar (Fig. 3a) or distinctly different zoning patterns (Fig. 3e). Subsequent magma mixing may disaggregate the crystal-rich mush, forming multi-cored Cpx macrocrysts (Fig. 3d and g). All early formed
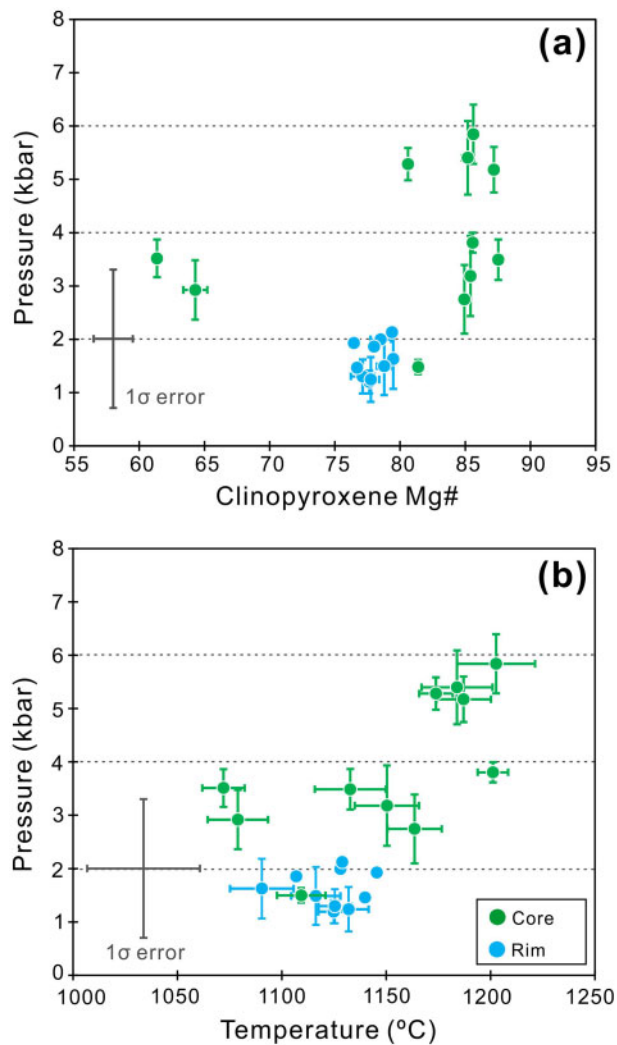
Fig. 19. Crystallization pressure for the cores and rims of the Cpx macrocrysts in the lamprophyre dyke. Temperature was calculated using the Cpx–melt thermometer of Putirka *et al.* (1996) and pressure was calculated using the Cpx–melt barometer of Putirka *et al.* (2003). The calculation results show that the cores crystallized from ~1·5 to 5·8 kbar and the rims crystallized from ~1 to 2 kbar (a). For the cores, the Cpx can be distinguished into three populations, i.e. ~5·4, ~3·3 and ~1·5 kbar (b). The rims are averaged to be ~1·6 kbar (b). One standard error of estimation values for the temperature and pressure are ±27 °C and ±1·3 kbar, respectively (Putirka *et al.*, 1996, 2003).

crystals that were transported into the shallower reservoir were finally equilibrated with the groundmass melt before eruption, resulting in a euhedral outline of the Cpx macrocrysts with similar Mg# in the rims (Fig. 5c).

The Cpx macrocrysts may have crystallized under different degrees of undercooling in the shallower reservoir, developing diverse zoning patterns that can be observed even at thin-section scale. The shallower reservoir may have high thermal gradients between the hot interior and cold margin (Fig. 20b). The cold margin may facilitate crystallization kinetics under variable degrees of undercooling (Welsch *et al.*, 2009; Shea & Hammer, 2013). The Cpx macrocrysts with coarse

layers (Fig. 3a) may have crystallized in the hot interior with very low degrees of undercooling, whereas those with Si–Mg-rich hourglass sector zoning (Fig. 10) may have crystallized from the margin with relatively low degrees of undercooling. The concentric Cr-rich and Cr-poor layers in the sector-zoned crystals were developed as a result of magma mixing. The closely packed layers with straight boundaries are distributed in the Si–Mg-rich sectors (Fig. 13a) and thus they also formed as a result of crystallization kinetics. The closely packed layers with wavy boundaries show concentric Cr-rich and Cr-poor layers (Fig. 13c), and they formed by rapid crystal movement through thermal and chemical gradients. Frequent crystal movement between the hot interior and cold margin caused by magma convection may lead to the formation of either concentric layers or closely packed fine layers in these Cpx macrocrysts. The sieve texture and patchy zoning (Fig. 4c) of the Cpx macrocrysts are attributed to the partial dissolution of early formed core by the groundmass melt at late stage.

The magma plumbing and storage system revealed for the ultrapotassic lamprophyre dyke in this study indicates that volumetrically minor ultrapotassic magmas may experience complex magma history in the crust before eruption. The ultrapotassic magmatic system in our model involves multiple magma reservoirs, which is consistent with the common observation for volatile-rich alkaline magmas (e.g. Mt. Etna and Stromboli in Italy), where many magma reservoirs are present at variable depths of crust (Francalanci *et al.*, 2005; Ubide *et al.*, 2019a, 2019b). This study highlights that ultrapotassic magmas could be a mixture of compositionally variable magmas derived from different mantle sources and thus the evolution of the magmas in a transcrustal magmatic system should play a significant role in the compositions of minerals and rocks.

CONCLUSIONS

The Cpx macrocrysts of the lamprophyre dyke in the Kyrgyz North Tianshan orogen display complex oscillatory zoning patterns, which record periodic mixing of magmas derived from different mantle sources in a transcrustal magmatic system. Multiple Cpx populations that crystallized from different deeper magma reservoirs were transported into a shallower magma reservoir and mixed along with their host magmas. Progressive recharging of magmas from different magma reservoirs resulted in the periodic change of magma compositions. Diverse textural and chemical zoning patterns of the Cpx macrocrysts imply variable degrees of undercooling within the magma reservoirs. Concurrent mixing and crystallization of Cpx from the hot interior of the magma reservoir may develop coarse layers with obvious resorption surfaces in the zoning patterns, whereas crystallization from the cold margin may result in the cryptic sector zoning and the closely packed fine layers with straight boundaries. Rapid crystal movement through thermal and chemical gradients
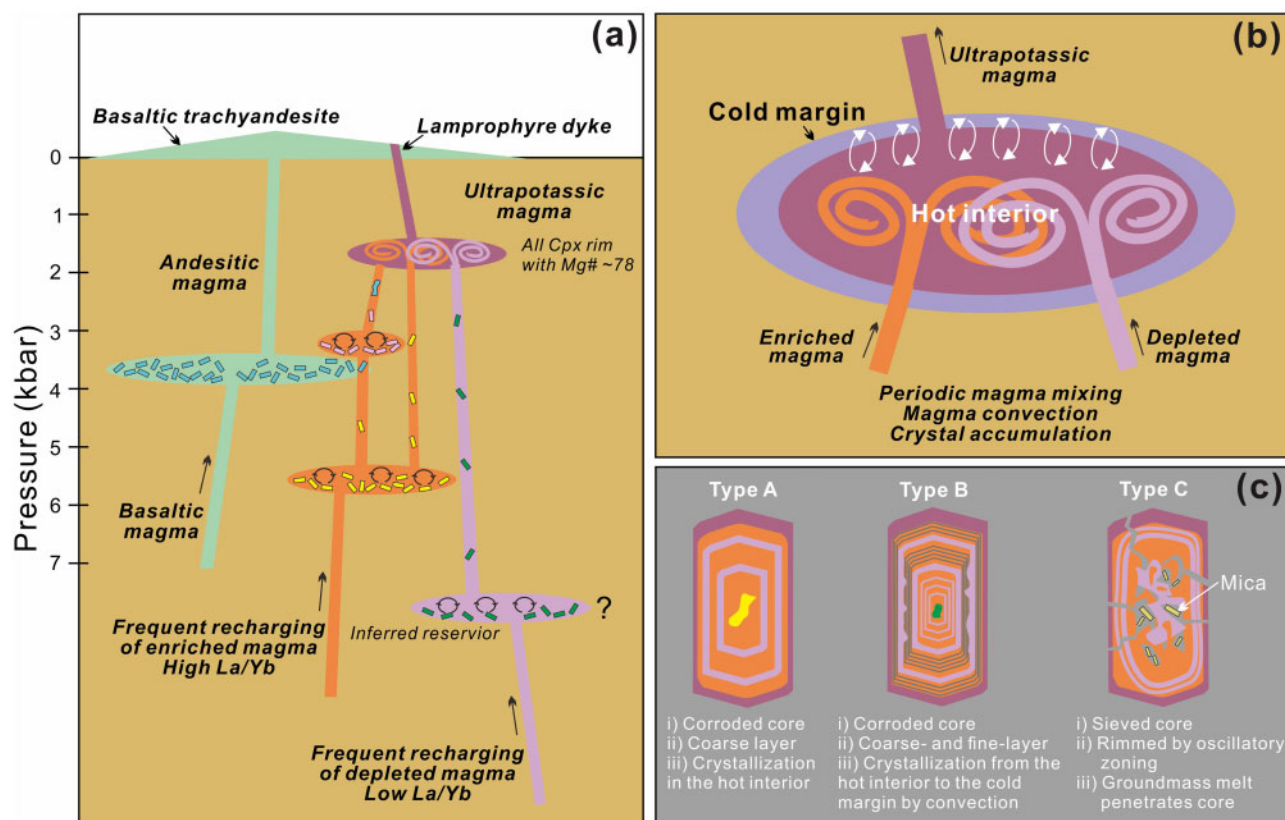
Fig. 20. Schematic diagrams showing a possible transcrustal magmatic system for the ultrapotassic lamprophyre dyke (a), crystallization of Cpx in the shallow magma reservoir with variable degrees of undercooling (b) and typical zoning patterns of the Cpx macrocrysts (c) in the lamprophyre dyke. (b) is modified after Welsch *et al.* (2009). (See details in the text.) Diagrams are not to scale.

resulted in the closely packed fine layers with wavy boundaries. This study demonstrates that the ultrapotassic magmas may be produced by mixing of magmas from different mantle sources and may have experienced complex thermodynamic processes in a transcrustal magmatic system during ascent.

SUPPLEMENTARY DATA

Supplementary data are available at *Journal of Petrology* online.

REFERENCES

Ammannati, E., Jacob, D. E., Avanzinelli, R., Foley, S. F. & Conticelli, S. (2016). Low Ni olivine in silica-undersaturated ultrapotassic igneous rocks as evidence for carbonate metasomatism in the mantle. *Earth and Planetary Science Letters* **444**, 64–74.

Biske, Y. S., Konopelko, D. L. & Seltmann, R. (2013). Geodynamics of late Paleozoic magmatism in the Tien Shan and its framework. *Geotectonics* **47**, 291–309.

Blundy, J. D., Falloon, T. J., Wood, B. J. & Dalton, J. A. (1995). Sodium partitioning between clinopyroxene and silicate melts. *Journal of Geophysical Research: Solid Earth* **100**, 15501–15515.

Cao, Y., Mikolaichuk, A. V., Xie, W. & Wang, C. Y. (2019). An early Devonian intra-plate bimodal volcanic suite in the Kyrgyz North Tianshan belt, the central Asian orogenic belt. *Journal of Asian Earth Sciences* **179**, 21–36.

Cashman, K. V., Sparks, R. S. J. & Blundy, J. D. (2017). Vertically extensive and unstable magmatic systems: a unified view of igneous processes. *Science* **355**, eaag3055.

Catanzaro, E. J., Murphy, T. J., Garner, E. L. & Shields, W. R. (1969). Absolute isotopic abundance ratio and atomic weight of terrestrial rubidium. *Journal of Research of the National Bureau of Standards Section A—Physics and Chemistry* **73**, 511–516.

Clark, A. H., Pearce, T. H., Roeder, P. L. & Wolfson, I. (1986). Oscillatory zoning and other microstructures in magmatic olivine and augite: Nomarski interference contrast observations on etched polished surfaces. *American Mineralogist* **71**, 734–741.

Conticelli, S. & Peccerillo, A. (1992). Petrology and geochemistry of potassic and ultrapotassic volcanism in central Italy: petrogenesis and inferences on the evolution of the mantle sources. *Lithos* **28**, 221–240.

Cooper, K. M. (2017). What does a magma reservoir look like? The "crystal's-eye" view. *Elements* **13**, 23–28.

Djenchuraeva, R. D. (2005). *Geodynamics and Metallogeny of Active Continental Margins of the Kyrgyz Tien Shan*. Berlin: Springer, pp. 1309–1311.

Downes, M. J. (1974). Sector and oscillatory zoning in calcic augites from M. Etna, Sicily. *Contributions to Mineralogy and Petrology* **47**, 187–196.

Duggen, S., Hoernle, K., Van Den Bogaard, P. & Garbe-Schönberg, D. (2005). Post-collisional transition from subduction- to intraplate-type magmatism in the westernmost Mediterranean: evidence for continental-edge delamination of subcontinental lithosphere. *Journal of Petrology* **46**, 1155–1201.

Elardo, S. & Shearer, C., Jr (2014). Magma chamber dynamics recorded by oscillatory zoning in pyroxene and olivine phenocrysts in basaltic lunar meteorite Northwest Africa 032. *American Mineralogist* **99**, 355–368.

Elburg, M., Vroon, P., van der Wagt, B. & Tchalikian, A. (2005). Sr and Pb isotopic composition of five USGS glasses (BHVO-2G, BIR-1G, BCR-2G, TB-1G, NKT-1G). *Chemical Geology* **223**, 196–207.

Eriksson, S. C. (1985). Oscillatory zoning in clinopyroxenes from the Guide Copper Mine, Phalaborwa, South Africa. *American Mineralogist* **70**, 74–79.

Foley, S. (1992a). Petrological characterization of the source components of potassic magmas: geochemical and experimental constraints. *Lithos* **28**, 187–204.

Foley, S. (1992b). Vein-plus-wall-rock melting mechanisms in the lithosphere and the origin of potassic alkaline magmas. *Lithos* **28**, 435–453.

Foley, S. F., Venturelli, G., Green, D. H. & Toscani, L. (1987). The ultrapotassic rocks: characteristics, classification, and constraints for petrogenetic models. *Earth-Science Reviews* **24**, 81–134.

Francalanci, L., Davies, G. R., Lustenhouwer, W., Tommasini, S., Mason, P. R. D. & Conticelli, S. (2005). Intra-grain Sr isotope evidence for crystal recycling and multiple magma reservoirs in the recent activity of Stromboli Volcano, Southern Italy. *Journal of Petrology* **46**, 1997–2021.

Ginibre, C. & Wörner, G. (2007). Variable parent magmas and recharge regimes of the Parinacota magma system (N. Chile) revealed by Fe, Mg and Sr zoning in plagioclase. *Lithos* **98**, 118–140.

Ginibre, C., Kronz, A. & Wörner, G. (2002a). High-resolution quantitative imaging of plagioclase composition using accumulated backscattered electron images: new constraints on oscillatory zoning. *Contributions to Mineralogy and Petrology* **142**, 436–448.

Ginibre, C., Wörner, G. & Kronz, A. (2002b). Minor- and trace-element zoning in plagioclase: implications for magma chamber processes at Parinacota volcano, northern Chile. *Contributions to Mineralogy and Petrology* **143**, 300–315.

Ginibre, C., Worner, G. & Kronz, A. (2007). Crystal zoning as an archive for magma evolution. *Elements* **3**, 261–266.

Goto, A. & Tatsumi, Y. (1996). Quantitative analysis of rock samples by an X-ray fluorescence spectrometer (II). *Rigaku Journal* **13**, 20–39.

Gülmez, F., Genç, Ş. C., Prelević, D., Tüysüz, O., Karacik, Z., Roden, M. F. & Billor, Z. (2016). Ultrapotassic volcanism from the waning stage of the Neotethyan subduction: a key study from the Izmir–Ankara–Erzincan suture belt, Central Northern Turkey. *Journal of Petrology* **57**, 561–593.

Han, B.-F., He, G.-Q., Wang, X.-C. & Guo, Z.-J. (2011). Late Carboniferous collision between the Tarim and Kazakhstan–Yili terranes in the western segment of the South Tian Shan Orogen, Central Asia, and implications for the Northern Xinjiang, western China. *Earth-Science Reviews* **109**, 74–93.

Huang, X.-L., Niu, Y., Xu, Y.-G., Chen, L.-L. & Yang, Q.-J. (2010). Mineralogical and Geochemical constraints on the petrogenesis of post-collisional potassic and ultrapotassic rocks from Western Yunnan. *Journal of Petrology* **51**, 1617–1654.

Humphreys, M. C. S., Blundy, J. D. & Sparks, R. S. J. (2006). Magma evolution and open-system processes at Shiveluch volcano: insights from phenocryst zoning. *Journal of Petrology* **47**, 2303–2334.

Jennings, E. S., Gibson, S. A., Maclennan, J. & Heinonen, J. S. (2017). Deep mixing of mantle melts beneath continental flood basalt provinces: constraints from olivine-hosted melt inclusions in primitive magmas. *Geochimica et Cosmochimica Acta* **196**, 36–57.

Konopelko, D., Seltmann, R., Apayarov, F., Belousova, E., Izokh, A. & Lepekhina, E. (2013). U–Pb–Hf zircon study of two mylonitic granite complexes in the Talas–Fergana fault zone, Kyrgyzstan, and Ar–Ar age of deformations along the fault. *Journal of Asian Earth Sciences* **73**, 334–346.

Liang, X., Wei, G., Li, X. H. & Liu, Y. (2003). Precise measurement of $^{143}Nd/^{144}Nd$ and Sm/Nd ratios using multiple-collectors inductively couple plasma-mass spectrometer (MC-ICP-MS). *Geochimica* **32**, 91–96 [in Chinese with English abstract].

Lin, J., Liu, Y., Yang, Y. & Hu, Z. (2016). Calibration and correction of LA-ICP-MS and LA-MC-ICP-MS analyses for element contents and isotopic ratios. *Solid Earth Sciences* **1**, 5–27.

Lissenberg, C. J. & MacLeod, C. J. (2016). A reactive porous flow control on mid-ocean ridge magmatic evolution. *Journal of Petrology* **57**, 2195–2220.

Liu, Y., Hu, Z., Gao, S., Günther, D., Xu, J., Gao, C. & Chen, H. (2008). *In situ* analysis of major and trace elements of anhydrous minerals by LA-ICP-MS without applying an internal standard. *Chemical Geology* **257**, 34–43.

Lofgren, G. E., Huss, G. R. & Wasserburg, G. J. (2006). An experimental study of trace-element partitioning between Ti–Al-clinopyroxene and melt: equilibrium and kinetic effects including sector zoning. *American Mineralogist* **91**, 1596–1606.

Maclennan, J. (2008). Concurrent mixing and cooling of melts under Iceland. *Journal of Petrology* **49**, 1931–1953.

Martin, V. M., Davidson, J., Morgan, D. & Jerram, D. A. (2010). Using the Sr isotope compositions of feldspars and glass to distinguish magma system components and dynamics. *Geology* **38**, 539–542.

Masotta, M., Pontesilli, A., Mollo, S., Armienti, P., Ubide, T., Nazzari, M. & Scarlato, P. (2020). The role of undercooling during clinopyroxene growth in trachybasaltic magmas: Insights on magma decompression and cooling at Mt. Etna volcano. *Geochimica et Cosmochimica Acta* **268**, 258–276.

McDonough, W. (1990). Constraints on the composition of the continental lithospheric mantle. *Earth and Planetary Science Letters* **101**, 1–18.

McDonough, W. F. & Sun, S. S. (1995). The composition of the Earth. *Chemical Geology* **120**, 223–253.

McKenzie, D. A. N. & O'Nions, R. K. (1991). Partial melt distributions from inversion of rare earth element concentrations. *Journal of Petrology* **32**, 1021–1091.

Miller, C., Schuster, R., Klötzli, U., Frank, W. & Purtscheller, F. (1999). Post-collisional potassic and ultrapotassic magmatism in SW Tibet: geochemical and Sr–Nd–Pb–O isotopic constraints for mantle source characteristics and petrogenesis. *Journal of Petrology* **40**, 1399–1424.

Mollo, S., Del Gaudio, P., Ventura, G., Iezzi, G. & Scarlato, P. (2010). Dependence of clinopyroxene composition on cooling rate in basaltic magmas: Implications for thermobarometry. *Lithos* **118**, 302–312.

Mollo, S., Putirka, K., Misiti, V., Soligo, M. & Scarlato, P. (2013). A new test for equilibrium based on clinopyroxene–melt pairs: clues on the solidification temperatures of Etnean alkaline melts at post-eruptive conditions. *Chemical Geology* **352**, 92–100.

Morimoto, N. (1988). Nomenclature of pyroxenes. *Mineralogy and Petrology* **39**, 55–76.

Muravyeva, N. S., Belyatsky, B. V., Senin, V. G. & Ivanov, A. V. (2014). Sr–Nd–Pb isotope systematics and clinopyroxene–host disequilibrium in ultra-potassic magmas from Toro-Ankole and Virunga, East-African Rift: implications for magma mixing and source heterogeneity. *Lithos* **210–211**, 260–277.

Neave, D. A. & Maclennan, J. (2020). Clinopyroxene dissolution records rapid magma ascent. *Frontiers in Earth Science* **8**, 188.

Neave, D. A., Passmore, E., Maclennan, J., Fitton, G. & Thordarson, T. (2013). Crystal–melt relationships and the record of deep mixing and crystallization in the AD 1783 Laki eruption, Iceland. *Journal of Petrology* **54**, 1661–1690.

Neave, D. A., Maclennan, J., Hartley, M. E., Edmonds, M. & Thordarson, T. (2014). Crystal storage and transfer in basaltic systems: the Skuggafjöll eruption, Iceland. *Journal of Petrology* **55**, 2311–2346.

Neave, D. A., Bali, E., Guðfinnsson, G. H., Halldórsson, S. A., Kahl, M., Schmidt, A.-S. & Holtz, F. (2019). Clinopyroxene–liquid equilibria and geothermobarometry in natural and experimental tholeiites: the 2014–2015 Holuhraun eruption, Iceland. *Journal of Petrology* **60**, 1653–1680.

Nelson, S. T. & Montana, A. (1992). Sieve-textured plagioclase in volcanic rocks produced by rapid decompression. *American Mineralogist* **77**, 1242–1249.

O'Brien, H., Irving, A. & McCallum, I. (1988). Complex zoning and resorption of phenocrysts in mixed potassic mafic magmas of the Highwood Mountains, Montana. *American Mineralogist* **73**, 1007–1024.

Owen, J. P. (2008). Geochemistry of lamprophyres from the Western Alps, Italy: implications for the origin of an enriched isotopic component in the Italian mantle. *Contributions to Mineralogy and Petrology* **155**, 341–362.

Pan, S., Zheng, J. P., Yin, Z., Griffin, W., Xia, M., Lin, A. & Zhang, H. (2018). Spongy texture in mantle clinopyroxene records decompression-induced melting. *Lithos* **320–321**, 144–154.

Pearce, T. H. (1994). Recent work on oscillatory zoning in plagioclase. In: Parsons, I. (ed.) *Feldspars and their Reactions*. Dordrecht: Springer, pp. 313–349.

Petrone, C. M., Bugatti, G., Braschi, E. & Tommasini, S. (2016). Pre-eruptive magmatic processes re-timed using a non-isothermal approach to magma chamber dynamics. *Nature Communications* **7**, 12946.

Petrone, C. M., Braschi, E., Francalanci, L., Casalini, M. & Tommasini, S. (2018). Rapid mixing and short storage timescale in the magma dynamics of a steady-state volcano. *Earth and Planetary Science Letters* **492**, 206–221.

Plank, T. & Langmuir, C. H. (1998). The chemical composition of subducting sediment and its consequences for the crust and mantle. *Chemical Geology* **145**, 325–394.

Pontesilli, A., Masotta, M., Nazzari, M., Mollo, S., Armienti, P., Scarlato, P. & Brenna, M. (2019). Crystallization kinetics of clinopyroxene and titanomagnetite growing from a trachybasaltic melt: new insights from isothermal time-series experiments. *Chemical Geology* **510**, 113–129.

Prelević, D., Foley, S. F., Cvetković, V. & Romer, R. L. (2004). Origin of minette by mixing of lamproite and dacite magmas in Veliki Majdan, Serbia. *Journal of Petrology* **45**, 759–792.

Prelević, D., Foley, S. F., Romer, R. L., Cvetković, V. & Downes, H. (2005). Tertiary ultrapotassic volcanism in Serbia: constraints on petrogenesis and mantle source characteristics. *Journal of Petrology* **46**, 1443–1487.

Prelević, D., Foley, S. F., Romer, R. & Conticelli, S. (2008). Mediterranean Tertiary lamproites derived from multiple source components in postcollisional geodynamics. *Geochimica et Cosmochimica Acta* **72**, 2125–2156.

Prelević, D., Akal, C., Foley, S. F., Romer, R. L., Stracke, A. & Van Den Bogaard, P. (2012). Ultrapotassic mafic rocks as geochemical proxies for post-collisional dynamics of orogenic lithospheric mantle: the case of Southwestern Anatolia. *Journal of Petrology* **53**, 1019–1055.

Putirka, K. D. (2008). Thermometers and barometers for volcanic systems. *Reviews in Mineralogy and Geochemistry* **69**, 61–120.

Putirka, K., Johnson, M., Kinzler, R., Longhi, J. & Walker, D. (1996). Thermobarometry of mafic igneous rocks based on clinopyroxene–liquid equilibria, 0–30 kbar. *Contributions to Mineralogy and Petrology* **123**, 92–108.

Putirka, K., Mikaelian, H., Ryerson, F. & Shaw, H. (2003). New clinopyroxene–liquid thermobarometers for mafic, evolved, and volatile-bearing lava compositions, with applications to lavas from Tibet and the Snake River Plain, Idaho. *American Mineralogist* **88**, 1542–1554.

Qi, L. & Grégoire, D. C. (2000). Determination of trace elements in twenty six Chinese geochemistry reference materials by inductively coupled plasma-mass spectrometry. *Geostandards Newsletter* **24**, 51–63.

Qi, L., Hu, J. & Grégoire, D. C. (2000). Determination of trace elements in granites by inductively coupled plasma mass spectrometry. *Talanta* **51**, 507–513.

Rock, N. M. S. (1977). The nature and origin of lamprophyres: some definitions, distinctions, and derivations. *Earth-Science Reviews* **13**, 123–169.

Rock, N. M. S. (1984). Nature and origin of calc-alkaline lamprophyres: minettes, vogesites, kersantites and spessartites. *Transactions of the Royal Society of Edinburgh: Earth Sciences* **74**, 193–227.

Rock, N. M. S. (1986). The nature and origin of ultramafic lamprophyres: alnöites and allied rocks. *Journal of Petrology* **27**, 155–196.

Rock, N. M. S. (1987). The nature and origin of lamprophyres: an overview. In: Fitton, J. G. & Upton, B. G. J. (eds) *Alkaline Lgneous Rocks. Geological Society, London, Special Publications* **30**, 191–226.

Rock, N. M. S. (1991). *Lamprophyres*. Glasgow: Blackie, 285 pp.

Rudge, J. F., Maclennan, J. & Stracke, A. (2013). The geochemical consequences of mixing melts from a heterogeneous mantle. *Geochimica et Cosmochimica Acta* **114**, 112–143.

Shaw, D. M. (1970). Trace element fractionation during anatexis. *Geochimica et Cosmochimica Acta* **34**, 237–243.

Shea, T. & Hammer, J. E. (2013). Kinetics of cooling- and decompression-induced crystallization in hydrous

mafic–intermediate magmas. *Journal of Volcanology and Geothermal Research* **260**, 127–145.

Shimizu, N. (1990). The oscillatory trace element zoning of augite phenocrysts. *Earth-Science Reviews* **29**, 27–37.

Shore, M. & Fowler, A. D. (1996). Oscillatory zoning in minerals; a common phenomenon. *Canadian Mineralogist* **34**, 1111–1126.

Singer, B. S., Dungan, M. A. & Layne, G. D. (1995). Textures and Sr, Ba, Mg, Fe, K and Ti compositional profiles in volcanic plagioclase: clues to the dynamics of calc-alkaline magma chambers. *American Mineralogist* **80**, 776–798.

Soder, C. G. & Romer, R. L. (2018). Post-collisional potassic–ultrapotassic magmatism of the Variscan orogen: implications for mantle metasomatism during continental subduction. *Journal of Petrology* **59**, 1007–1034.

Sparks, R. S. J. & Cashman, K. V. (2017). Dynamic magma systems: implications for forecasting volcanic activity. *Elements* **13**, 35–40.

Stewart, M. L. & Pearce, T. H. (2004). Sieve-textured plagioclase in dacitic magma: Interference imaging results. *American Mineralogist* **89**, 348–351.

Streck, M. J. (2008). Mineral textures and zoning as evidence for open system processes. *Reviews in Mineralogy and Geochemistry* **69**, 595–622.

Sun, S.-S. & McDonough, W. F. (1989). Chemical and isotopic systematics of oceanic basalts: implications for mantle composition and processes. In: Saunders, A. D. & Norry, M. J. (eds) *Magmatism in the Ocean Basins. Geological Society, London, Special Publications* **42**, 313–345.

Tomiya, A. & Takahashi, E. (2005). Evolution of the magma chamber beneath Usu volcano since 1663: a natural laboratory for observing changing phenocryst compositions and textures. *Journal of Petrology* **46**, 2395–2426.

Ubide, T., Galé, C., Arranz, E., Lago, M. & Larrea, P. (2014). Clinopyroxene and amphibole crystal populations in a lamprophyre sill from the Catalonian Coastal Ranges (NE Spain): a record of magma history and a window to mineral–melt partitioning. *Lithos* **184–187**, 225–242.

Ubide, T., Caulfield, J., Brandt, C., Bussweiler, Y., Mollo, S., Di Stefano, F., Nazzari, M. & Scarlato, P. (2019a). Deep magma storage revealed by multi-method elemental mapping of clinopyroxene megacrysts at Stromboli volcano. *Frontiers in Earth Science* **7**, 239.

Ubide, T., Mollo, S., Zhao, J.-X., Nazzari, M. & Scarlato, P. (2019b). Sector-zoned clinopyroxene as a recorder of magma history, eruption triggers, and ascent rates. *Geochimica et Cosmochimica Acta* **251**, 265–283.

Venturelli, G., Thorpe, R. S., Dal Piaz, G. V., Del Moro, A. & Potts, P. J. (1984). Petrogenesis of calc-alkaline, shoshonitic and associated ultrapotassic Oligocene volcanic rocks from the Northwestern Alps. *Contributions to Mineralogy and Petrology* **86**, 209–220.

Wei, G., Liang, X., Li, X. H. & Liu, Y. (2002). Precise measurement of Sr isotopic compositions of liquid and solid base using (LA) MCICP-MS. *Geochimica* **31**, 295–305 [in Chinese with English abstract].

Welsch, B., Faure, F., Bachèlery, P. & Famin, V. (2009). Microcrysts record transient convection at Piton de la Fournaise volcano (La Réunion hotspot). *Journal of Petrology* **50**, 2287–2305.

Winpenny, B. & Maclennan, J. (2011). A partial record of mixing of mantle melts preserved in Icelandic phenocrysts. *Journal of Petrology* **52**, 1791–1812.

Wood, B. & Blundy, J. (2003). Trace element partitioning under crustal and uppermost mantle conditions: the influences of ionic radius, cation charge, pressure, and temperature. In: Holland H. D. & Turekian, K. K. (eds.) *Treatise on Geochemistry* 2. Oxford: Elsevier, 395–424.

Yang, W.-B., Niu, H.-C., Shan, Q., Chen, H.-Y., Hollings, P., Li, N.-B., Yan, S. & Zartman, R. E. (2014). Geochemistry of primary-carbonate bearing K-rich igneous rocks in the Awulale Mountains, western Tianshan: implications for carbon-recycling in subduction zone. *Geochimica et Cosmochimica Acta* **143**, 143–164.

Zhang, L., Ren, Z.-Y., Wu, Y.-D. & Li, N. (2018). Strontium isotope measurement of basaltic glasses by laser ablation multiple collector inductively coupled plasma mass spectrometry based on a linear relationship between analytical bias and Rb/Sr ratios. *Rapid Communications in Mass Spectrometry* **32**, 105–112.